JGR Oceans

RESEARCH ARTICLE
10.1029/2021JC018056

Decadal Observations of Internal Wave Energy, Shear, and Mixing in the Western Arctic Ocean

Elizabeth C. Fine[1,2] **and Sylvia T. Cole**[1]

[1]Woods Hole Oceanographic Institution, Woods Hole, MA, USA, [2]Scripps Institution of Oceanography, La Jolla, CA, USA

Key Points:

- Over 100–300 m depth at daily and seasonal timescales, increasing near-inertial energy was associated with sea ice decline
- There is no evidence of increased turbulence over 100–300 m depth coincident with sea ice decline and the increase of near-inertial energy
- Sea ice conditions impact the vertical scales of internal wave energy, explaining why vertical mixing has not changed under sea ice decline

Correspondence to:
E. C. Fine,
efine@whoi.edu

Citation:
Fine, E. C., & Cole, S. T. (2022). Decadal observations of internal wave energy, shear, and mixing in the western Arctic Ocean. *Journal of Geophysical Research: Oceans*, *127*, e2021JC018056. https://doi.org/10.1029/2021JC018056

Received 30 SEP 2021
Accepted 2 MAR 2022

Abstract As Arctic sea ice declines, wind energy has increasing access to the upper ocean, with potential consequences for ocean mixing, stratification, and turbulent heat fluxes. Here, we investigate the relationships between internal wave energy, turbulent dissipation, and ice concentration and draft using mooring data collected in the Beaufort Sea during 2003–2018. We focus on the 50–300 m depth range, using velocity and CTD records to estimate near-inertial shear and energy, a finescale parameterization to infer turbulent dissipation rates, and ice draft observations to characterize the ice cover. All quantities varied widely on monthly and interannual timescales. Seasonally, near-inertial energy increased when ice concentration and ice draft were low, but shear and dissipation did not. We show that this apparent contradiction occurred due to the vertical scales of internal wave energy, with open water associated with larger vertical scales. These larger vertical scale motions are associated with less shear, and tend to result in less dissipation. This relationship led to a seasonality in the correlation between shear and energy. This correlation was largest in the spring beneath full ice cover and smallest in the summer and fall when the ice had deteriorated. When considering interannually averaged properties, the year-to-year variability and the short ice-free season currently obscure any potential trend. Implications for the future seasonal and interannual evolution of the Arctic Ocean and sea ice cover are discussed.

Plain Language Summary Changes in the Arctic climate have resulted in less summertime Arctic sea ice. These changes in ice-cover have the potential to influence internal waves, which carry energy deep into the ocean, providing the energy source for most ocean mixing. In this study, we use 15 years of observations to assess how changes in sea ice are related to changes in both the internal wavefield and the turbulent mixing caused by internal wave breaking. We find that while sea ice decline creates a more energetic internal wavefield, the mixing that internal waves causes doesn't increase in ice-free conditions. We show that this apparent contradiction occurs because in ice-free conditions the internal wavefield tends to consist of waves with larger vertical scale that are less prone to breaking, so that even though the total energy increases, these more-energetic waves don't increase total ocean mixing. This mechanism serves to protect sea ice from accelerating decline that could occur if sea ice loss resulted in more ocean mixing and thus higher oceanic heat fluxes.

1. Introduction

In the last several decades, the ice cover of the Arctic Ocean has declined dramatically (Perovich et al., 2020; Stroeve et al., 2012). This decrease in ice cover provides more direct access for wind energy and momentum to the upper ocean. At large scales, these changes have important implications for circulation, freshwater storage, and the energy transmitted to mesoscale eddies (Armitage et al., 2020). At smaller scales, changes in sea ice have the potential to affect ocean mixing processes. Wind stress can force mixed layer motions that can result in vertically propagating near-inertial internal waves (Gill, 1984). In the global ocean away from topography, internal waves provide the main source of energy for diapycnal mixing. As the ice cover becomes less extensive, many have suggested the potential for increased near-inertial energy and shear, and resulting increased vertical mixing within the ocean (Dosser & Rainville, 2016; Martini et al., 2014; Pinkel, 2005; Rainville & Woodgate, 2009).

Stratification in the western Arctic Ocean is largely controlled by salinity, so that heat is stored in subsurface reservoirs (Aagaard et al., 1981; Timmermans et al., 2017). Ocean mixing rates influence the release of heat from these reservoirs. Upward heat fluxes are determined by the characteristics of the source waters that feed the reservoirs, the details of the subduction processes that ventilate these depths, and the diapycnal mixing that drives vertical heat fluxes (MacKinnon et al., 2021; Timmermans et al., 2018). Generally, the strong halocline persists

due to relatively weak diapycnal mixing (Shaw et al., 2009; Toole et al., 2010). If the internal wavefield becomes more energetic as a result of increased surface forcing, the dissipation of this energy at small scales could result in elevated diapycnal mixing rates (Rainville et al., 2011). Higher mixing rates would increase the vertical transport of subducted heat to the sea surface, with implications for sea ice and the atmosphere. Over time, long-term increases in mixing rates could weaken the halocline stratification and further increase the vertical transport of oceanic heat to the sea ice (Carmack et al., 2015).

Due to the Arctic's subsurface heat, a wind-ice-ocean feedback cycle mediated by internal waves could become increasingly important (Dosser et al., 2021; Gimbert et al., 2012; Rainville et al., 2011; Rainville & Woodgate, 2009). This feedback cycle has three steps, as follows:

1. A decline in sea ice concentration or ice draft increases the energy and momentum transmitted into the upper ocean in the form of inertial oscillations. These inertial oscillations generate near-inertial internal waves, which carry energy to the ocean interior.
2. Increased internal wave energy in the upper ocean cascades to increasingly small spatial and temporal scales, eventually leading to turbulent dissipation and higher diapycnal mixing rates.
3. Due to the presence of upper ocean heat reservoirs, specifically Atlantic Water and Pacific Summer Water, increased diapycnal mixing drives upward vertical heat fluxes that melt more sea ice. These vertical heat fluxes thus accelerate sea ice decline, reducing sea ice concentration and draft, starting the cycle again.

This cycle could interact with other feedback cycles. For instance, once sea ice is melted by oceanic heat fluxes, the open water has a lower albedo than ice, resulting in ice-albedo feedback.

Some pieces of this feedback cycle have already been observed. Studies in Arctic shelf seas, where internal waves can penetrate to full-depth, show that internal wave energy is generally higher in open water conditions relative to ice covered oceans (Lenn et al., 2011; Martini et al., 2014; Rainville & Woodgate, 2009). In the interior Arctic, there is observational evidence that near-inertial internal waves are both increasing in amplitude and becoming more variable, increasing the likelihood of wave amplitudes that are large enough to trigger turbulent mixing (Dosser & Rainville, 2016). Limited observations suggest isolated events with higher NIW energy may be linked to modestly elevated mixing in the upper western Arctic water column (Fine et al., 2021).

The internal wavefield is a major source of energy for ocean mixing, so that regions with more energetic internal wavefields generally have higher rates of turbulent dissipation and diffusivity (see e.g., Waterhouse et al. (2014)). However, so far elevated mixing in response to sea ice decline has not been broadly observed in the western Arctic outside of shelf seas (Dosser et al., 2021; Guthrie et al., 2013; Lincoln et al., 2016; Rippeth et al., 2015). In contrast, in some regions of the eastern Arctic there is evidence that sea ice decline is leading to increased vertical heat fluxes from warm subsurface Atlantic Water thereby accelerating sea ice melt (Polyakov et al., 2020).

The Arctic internal wavefield is unique for a number of reasons. Sea ice affects both the initial generation of internal waves (McPhee, 2012; Morison et al., 1985) and their ability to reflect off the ocean's upper boundary due to dissipation within the ice-ocean boundary layer (Pinkel, 2005). Sea ice concentration and roughness both influence the mean ice-ocean drag coefficient, determining how efficiently momentum is carried into the mixed layer, with rougher ice associated with higher drag and maximum drag coefficient occurring for ice concentrations around 80% (Cole et al., 2017, 2018; Lu et al., 2011; Martin et al., 2014). The high-latitude of the Arctic Ocean means that the semi-diurnal tide is sub-inertial and thus is confined to evanescent waves along topography in much of the basin. Double diffusive layers are persistently found at depth in the western Arctic, and these layers may result in reflection and/or refraction of propagating internal waves (Ghaemsaidi et al., 2016; Sutherland, 2016). Overall, the combination of weak internal tides, weaker storm tracks, shallow mixed layer depths, the presence of sea ice, and the weak gradient of the Coriolis frequency with latitude result in an Arctic internal wavefield that is weaker than at midlatitudes (Guthrie & Morison, 2021; Morison et al., 1985; Pinkel, 2005).

In the current work we focus on a single mooring site in the western Arctic, where the area and time span of open water are increasing and warm Pacific Summer Water resides at shallow depths. In this region, Pacific-origin waters form an upper halocline, with relatively warm and fresher Pacific Summer Water usually found at depths shallower than 100 m and colder and saltier Pacific Winter Water beneath (Coachman & Barnes, 1961; Jackson et al., 2010; Steele et al., 2004; Timmermans et al., 2017). Atlantic Water is saltier still and persistently warm,

and at this site is usually found deeper than 300 m. The water depth at the study site is approximately 3,800 m and well away from topography, so the dynamics here represent the Arctic interior rather than the shelf seas where full depth penetration by near-inertial waves occurs. The current study is concerned with depths above 300 m, as double diffusive convection plays an increased role in driving mixing beneath this depth (Shibley et al., 2017; Timmermans et al., 2008). Tides in this region are weak and not expected to be a strong source of energy for mixing (Kowalik & Proshutinsky, 2013), so we assume that wind-generated near-inertial waves are the primary energy source for turbulent dissipation and mixing. Understanding the response of the near-inertial wavefield to changing sea ice conditions thus provides insight into how the energy that drives most upper ocean turbulence and mixing is affected by changes in sea ice.

The primary goal of this study is to understand the key relationships, or lack thereof, between the sea ice cover, internal wave kinetic energy, internal wave shear, and parameterized mixing. Here, we simultaneously analyze these key variables in contrast to previous studies that focus on parameterized mixing with no consideration (Chanona et al., 2018; Dosser et al., 2021; Lique et al., 2014) or minimal consideration (Guthrie et al., 2013) of internal wave kinetic energy or shear. Similar to these previous studies, we find that turbulent dissipation rates at the mooring site from 2005 to 2018 do not statistically vary with sea ice concentration or draft, nor are they increasing in time. In contrast, we find that internal wave kinetic energy is influenced by ice concentration and draft at seasonal scales. This result is consistent with work by Dosser and Rainville (2016) that investigated internal wave amplitudes but not parameterized mixing. Here, the simultaneous analysis of internal wave energy and shear allows us to (a) investigate the differing response of internal wave energy and turbulent dissipation in a single study, and (b) advance a new explanation for why sea ice decline has such little impact on turbulent dissipation. Briefly, relative to ice free conditions, the presence of sea ice results in internal waves with weaker energy but higher vertical wavenumbers that are associated with more shear and dissipation.

In the sections that follow, we describe the 15 years mooring data record used in this study (Section 2) and the methods used to describe ice and ocean conditions and estimate turbulent dissipation and near-inertial velocities (Section 3). Interannual variability, seasonal cycles, and relationships between ice cover and ocean dynamics are described in Section 4, and discussed in Section 5. Throughout the analysis, we focus on the stratified depths above 300 m.

2. Data

The Beaufort Gyre Observing System (BGOS; e.g., Proshutinsky et al. (2019)) has deployed 3–4 moorings in the Beaufort Sea since 2003 (Figure 1). We analyze data from one, mooring A deployed at 75°N, 150°W (Figure 1), from 2003 to 2018 (Table 1). Of the four BGOS moorings, this location had the greatest number of ice-free days in each year and affords the best opportunity to consider the oceanic response to varying ice conditions. At the beginning of the data record ice was present at mooring A year round, while since 2007 the mooring site was frequently ice free in September. Since 2007, open water has occurred at mooring A in all years except 2010 and 2014, with 4–64 days of open water each year that occurred primarily in the late summer and early autumn.

2.1. Density and Velocity Profiles

The mooring was equipped with a McLane Moored Profiler (MMP) that profiled from approximately 50–2,050 m and collected hydrographic and velocity data. Velocity data from the MMP was gridded with 2 m vertical resolution (Figure 2b). MMP velocity profiles were missing from the August 2006 to August 2007, August 2008 to September 2009, August 2011 to August 2012, and October 2014 to October 2015 deployments (4 years of the 15 year record); periods without velocity measurements were not considered in the analysis (Table 1). In most years, these profiles were completed at alternating intervals of 6 hr and 2 days, a sampling scheme chosen so that the near inertial signal (associated with an approximately 12 hr period at this latitude) can be extracted while optimizing battery life over year-long deployments. During the 2017–2018 deployment the mooring was reconfigured so that depths above 250 m were sampled on a 3 hr basis, in addition to the standard sampling at depths below 250 m.

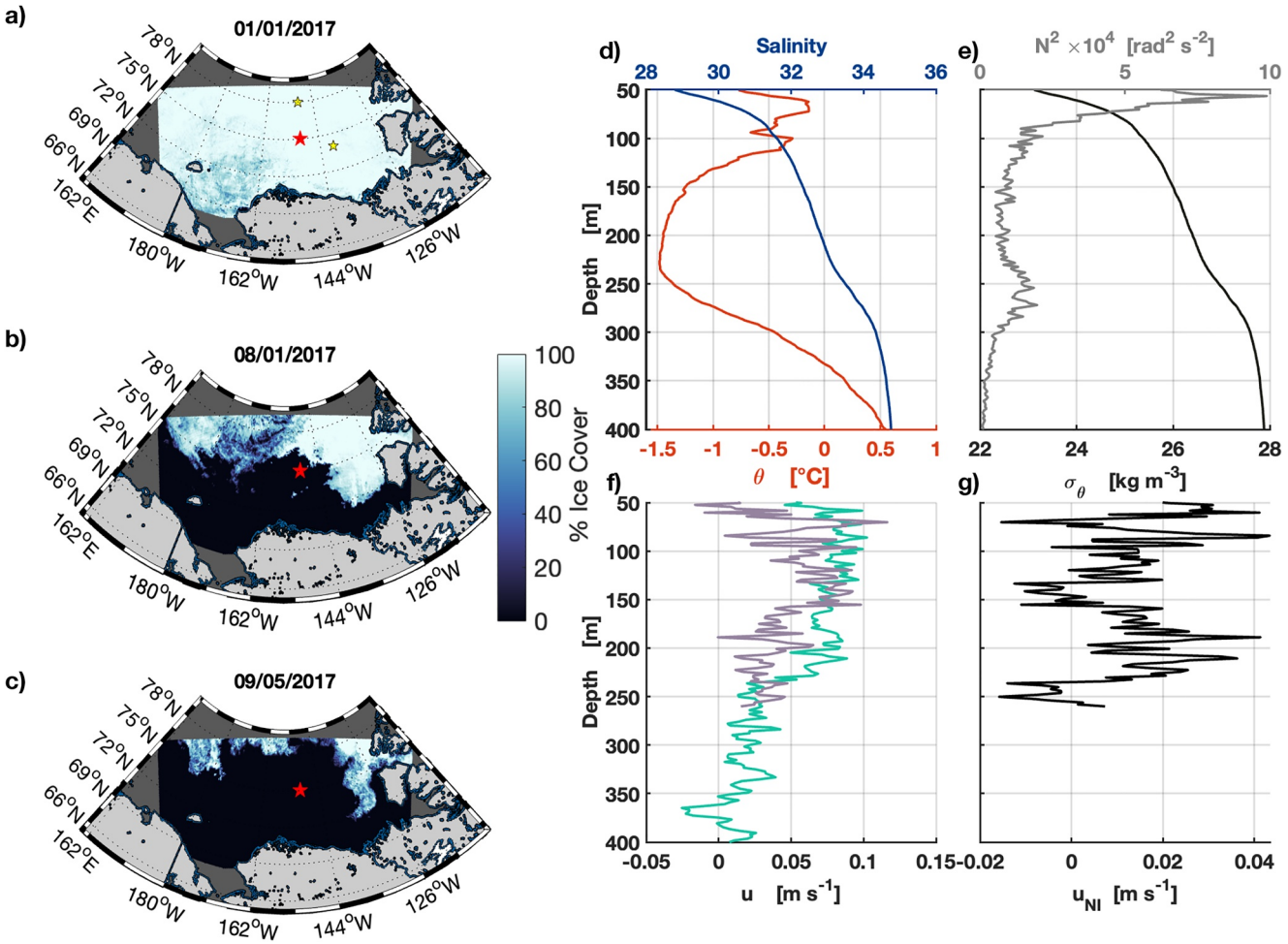

Figure 1. Example ice and ocean conditions. Beaufort Gyre Observing System mooring location A (red star) with Advanced Microwave Scanning Radiometer ice cover on (a) 1 January 2017, (b) 1 August 2017, and (c) 5 September 2017 (the date of the Arctic sea ice minimum). Locations of moorings B (north) and D (east) are shown as yellow stars in panel (a). Profiles in the upper 400 m taken on 1 August 2017 at mooring A of (d) salinity and temperature (e) potential density σ_θ and buoyancy frequency N^2 (f) 6 hr separated profiles of east-west velocity (g) near-inertial east-west velocity calculated by subtracting the mean of the two profiles from the teal profile.

3. Methods

3.1. Sea Ice Properties

An upward-looking sonar (ULS) is mounted at 50 m depth, and measures sea ice draft every 2 s (Krishfield et al. (2014)). In the analysis that follows, we refer to the daily mean of these measurements as "ice draft" (Figure 2a). Using daily median values rather than daily mean values does not substantially affect results.

Daily local sea ice concentration was approximated as the ratio of the number of 2-s ULS ice draft measurements that detect any ice draft to the total number of measurements for a given day (Figure 2a). Satellite ice concentration observed at 3 km scales from the Advanced Microwave Scanning Radiometer 2 satellite is compared to these data in Figure 5a, and generally agrees well (Melsheimer & Spreen, 2019; Spreen et al., 2008).

In parts of the analysis that follows, we bin data by both ice concentration and ice draft, with thresholds chosen based on the distribution of ice concentration and draft within the data set so that sufficient data was contained in each category for analysis. Ice cover is defined as "full" when daily ice concentration was greater than 99%, "ice free" when daily ice concentration was less than 5%, and "partial" for values in the range of 5%–99%. Data are binned by ice thickness only for days with "full" ice cover. "Thin" ice is defined as drafts less than 0.75 m, with "thick" ice having draft greater than 0.75 m. Our "thin ice" category approximately corresponds to the

Table 1
Beaufort Gyre Observing System Mooring A Deployments

Deployed	Recovered	# Profiles	Min pressure (dbar)
14 August 2003	10 August 2004	180	91
12 August 2004	9 August 2005	322	61
12 August 2005	17 August 2006	279	55
24 August 2006	6 August 2007	0	n/a
9 August 2007	27 July 2008	315	57
28 July 2008	29 September 2009	0	n/a
30 September 2009	28 September 2010	324	61
29 September 2010	29 July 2011	270	49
30 July 2011	11 August 2012	0	n/a
12 August 2012	13 August 2013	326	45
14 August 2013	30 September 2014	365	49
1 October 2014	5 October 2015	330[a]	49
7 October 2015	6 October 2016	326	41
7 October 2016	20 September 2017	308	47
24 September 2017	24 September 2018	2,694	43

[a]No velocity data was collected during this deployment.

World Meteorological Organization definitions of young ice and thin first-year ice, while our "thick ice" category includes medium and thick first-year ice, as well as multiyear ice (Krishfield et al., 2014; WMO, 1970). Conclusions were not qualitatively sensitive to the choice of thresholds for either ice concentration or draft. The number of profiles for each category is given in Table 2.

3.2. Velocity, Shear, and Derived Quantities

We utilize both synoptic velocity profiles and derived near-inertial velocity in this analysis as described below. In all velocity analyses, we exclude profiles containing mesoscale eddies. These were identified based on a threshold for velocity magnitude, $u^2 + v^2$. Profiles in which velocity magnitude exceeded 2×10^{-3} m^2 s^{-2} over a depth interval of at least 10 m were excluded. This threshold was chosen by eye to remove mesoscale signals while preserving near-inertial wave signals. Near-inertial waves and mesoscale eddies are generally cleanly separated, so that the results and conclusions were not sensitive to the choice of threshold provided it was sufficiently strict to remove the largest mesoscale events. At this stage, we also removed profiles with more than 25% of values missing in the target depth range (this usually occurred due to mooring knock down or when the MMP stopped profiling before the upper stop). We analyzed a total of 3,121 profiles, of which 830 were removed to avoid eddies (Table 2). Symbols used in the text for different velocity products are given in Table 3.

3.2.1. Wavenumber Spectra

Vertical wavenumber spectra were calculated from observed velocity. Prior to spectral analysis, Wentzel-Kramers-Brillouin (WKB) scaling and stretching were applied to velocity

$$U_{WKB} = \left(U(N_0/N(z,t))^{1/2}\right) \tag{1}$$

and the z-coordinate

$$dz^* = \int N_0^{-1} N(z,t) \tag{2}$$

to remove the influence of depth-varying stratification on vertical scales (Leaman & Sanford, 1975). Here, N_0 is the Garrett-Munk value of 5.2×10^{-3} rad s^{-1}, while $N(z, t)$ is a 4-day moving average of N at each depth (Garrett & Munk, 1972). Prior to calculating spectra, a Hamming window was applied over each 50–300 m profile to reduce edge effects.

Shear spectra were calculated by multiplying velocity spectra by $2\pi k_z$, in which k_z is the vertical wavenumber in the stretched coordinates. This approach produced results which were similar (although not identical and less noisy) to spectra obtained by first-differencing velocity to calculate shear and then taking spectra of shear directly. This approach eliminates the dependence on the somewhat arbitrary choice of scale for first-differencing.

Clockwise and counterclockwise rotating signals with depth were separated using rotary spectral decomposition applied to each profile (Gonella, 1972). Periodograms were derived for each velocity profile, and spectra were formed by averaging estimates at each vertical wavenumber. In general, vertical wavenumber spectra of shear are dominated by internal waves, as internal wave motions dominate variability at small vertical scales (Garrett & Munk, 1972).

3.2.2. Finescale Parameterization

We used the method described in Fine et al. (2021) to estimate the dissipation rate of turbulent kinetic energy (ϵ_{IW}) from moored shear and strain observations. We begin with the expression (Gregg, 1989; Kunze et al., 2006; Polzin et al., 1995; Whalen et al., 2015)

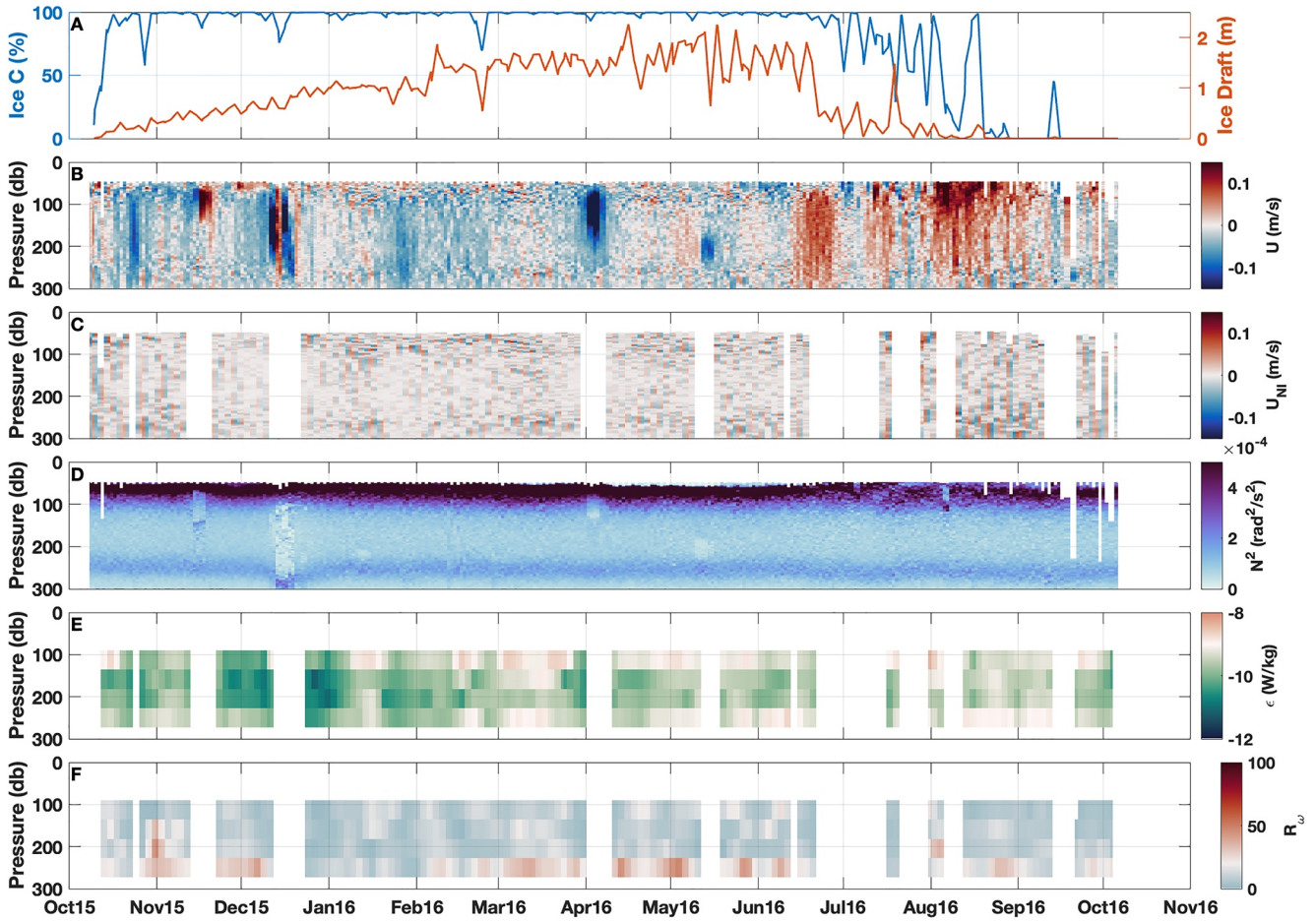

Figure 2. Example mooring data from September 2015-October 2016. (a) Ice concentration (blue) and draft (red). (b) Observed east-west velocity (U). (c) Near-inertially filtered velocity, with eddies removed (U_{NI}). (d) N^2. (e) ϵ_{IW} calculated from the finescale parameterization. (f) R_ω from the finescale parameterization.

Table 2
Number of Measurements by Ice Conditions, for All Upward-Looking Sonar (ULS) Measurements, All ULS Measurements That Coincided With McLane Moored Profiler Profiles in Which Near-Inertial Velocity Was Estimated, and All ULS Measurements for Which Near-Inertial Velocity Was Estimated, Excluding Profiles With Eddies

Ice conditions	All ULS	Concurrent NI	Eddies removed
Thick ice	3,137	1,706	1,289
Thin ice	641	386	291
Full ice	3,783	2,102	1,583
Partial ice	1,245	854	545
Ice free	403	165	88
Total	5,431	3,121	2,216

$$\epsilon_{IW} = \epsilon_0 \frac{\overline{N^2}}{N_0^2} \frac{\langle U_z^2 \rangle^2}{\langle U_{zGM}^2 \rangle} h_1(R_\omega) L(f, N) \tag{3}$$

in which $\epsilon_0 = 6.73 \times 10^{-10}$ W kg^{-1}, $N_0 = 5.2 \times 10^{-3}$ rad s^{-1}, $\langle U_z \rangle$ is finescale vertical shear calculated spectrally as described below, and $\langle U_{zGM}^2 \rangle$ is the variance of vertical shear from the Garrett and Munk 1976 model (Cairns & Williams, 1976; Garrett & Munk, 1972, 1975; Gregg & Kunze, 1991). Shear was scaled by the 4-day moving average of N, averaged within each depth window. The function h_1 is defined as

$$h_1(R_\omega) = \frac{3(R_\omega + 1)}{2\sqrt{2} R_\omega \sqrt{R_\omega - 1}}. \tag{4}$$

R_ω is the ratio of shear variance to that of strain,

$$R_\omega = \frac{\langle U_z^2 \rangle}{\overline{N^2} \langle \zeta_z^2 \rangle} \tag{5}$$

Table 3
Symbols Used for Velocity Products

Symbol	Description
U	Measured velocity
U_z	Measured shear
U_{zGM}	Garrett-Munk shear
U_{WKB}	WKB-scaled velocity
U_{zWKB}	WKB-scaled shear
U_{NI}	NI velocity
u_{NI}	NI velocity east-west component
v_{NI}	NI velocity north-south component

in which ζ represents isopycnal displacement. Strain (ζ_z) was calculated as $d\eta/dz$, in which η is the displacement of each isopycnal from the deployment mean. The latitudinal dependence $L(f, N)$ varies as

$$L(f,N) = \frac{f\cosh^{-1}\left(\frac{\overline{N}}{f}\right)}{f_{30}\cosh^{-1}\left(\frac{N_0}{f_{30}}\right)} \tag{6}$$

in which f is the Coriolis frequency and f_{30} is the Coriolis frequency at 30°, and represents the latitudinal dependence of the internal wavefield (Gregg et al., 2003). The finescale parameterization may be equivalently formulated with reference to strain as

$$\epsilon_{IW} = \epsilon_0 \frac{\overline{N^2}}{N_0^2} \frac{\left\langle \zeta_z^2 \right\rangle^2}{\left\langle \zeta_{zGM}^2 \right\rangle^2} h_2(R_\omega) L(f,N), \tag{7}$$

in which the scaling h_2 is given by

$$h_2(R_\omega) = \frac{R_\omega(R_\omega+1)}{6\sqrt{2}\sqrt{R_\omega - 1}}. \tag{8}$$

While many assumptions go into this finescale parameterization, this method has demonstrated remarkable success in the global ocean (Polzin et al., 2014; Whalen et al., 2015). Limited observational studies suggest the parameterization also applies well to the Arctic Ocean (Chanona et al., 2018; Fer, 2014; Fine et al., 2021; Guthrie et al., 2013), in spite of an internal wavefield that is much weaker than the midlatitudes due to weak internal tides, weaker storm tracks, shallow mixed layer depths, the presence of sea ice, and limited variation of the Coriolis frequency with latitude (Guthrie & Morison, 2021; Morison et al., 1985; Pinkel, 2005). The use of finescale parameterizations in the Arctic is restricted by the presence of persistent double diffusive convection within the Atlantic Water halocline, which cannot be successfully parameterized within the finescale paradigm. The finescale parameterization also does not apply in the pycnocline where density changes rapidly with depth. Thus, we restricted its use to the stratified depths beneath the pycnocline and above 300 m, below which diffusive layers are common. Above 300 m double diffusive steps are rare (we visually identified double diffusive steps in less than 1% of profiles during three representative years). We applied the finescale parameterization over four overlapping depth windows: 75–150, 100–200, 150–250, and 200–300 m. Variance in both shear ($\langle U_z^2 \rangle$) and strain ($\langle \zeta_z^2 \rangle$) were calculated from spectra of the shear and strain taken as first differences over the 2-m bins. Strain and shear were detrended and windowed using a Hamming window prior to calculating Fourier coefficients. Shear spectra were corrected by a sinc^2 function to account for the McLane profiler 2-m binning (Polzin et al., 2002). Spectra were calculated for individual profiles and then averaged over 4-day temporal windows to reduce noise in ϵ_{IW} estimates. We estimated variance by integrating spectra from the lowest wavenumber to a cutoff. The high-wavenumber cutoff of 0.05 cpm (corresponding to a 20-m wavelength) was chosen to retain sufficient wavenumber range for the integration while avoiding small scales where white noise in velocity causes a linear rise in shear spectra.

3.2.3. Near-Inertial Velocity, Shear, and Horizontal Kinetic Energy

To estimate the near-inertial signal from the observed velocity data, profiles with 6 hr temporal separation were paired. As each pair of profiles was separated by approximately half an inertial period, near-inertial velocity is estimated as the velocity signal at each measurement subtracted from the mean velocity of the pair (Leaman & Sanford, 1975; Silverthorne & Toole, 2009). The near-inertial velocity estimate, (U_{NI}), mostly consists of near-inertial internal waves, which dominate the internal wave signal at this location. Near-inertial shear (U_{zNI}) was calculated as the first-difference of near-inertial velocity over 2-m scales. While this small scale for first differencing results in some noise in the resulting shear, results are calculated from means or medians of shear in depth, and are not meaningfully affected by the choice of scale for first differencing. Velocity data from 2017 to 2018, which was sampled at 3 hr frequency, was down-sampled to match the sampling rate from the earlier years prior to calculating U_{NI} to avoid heavily weighting this 1 year's worth of data. This temporal method of isolating the near-inertial signal is distinct from the approach employed by the finescale parameterization, in

which the high-wavenumber component of full velocity profiles were isolated to estimate turbulent dissipation. Near-inertial horizontal kinetic energy density (referred to throughout as "near-inertial energy") was calculated as $HKE_{NI} = 0.5\left(u_{NI}^2 + v_{NI}^2\right)$. The 6 hr sampling scheme results in some aliasing of the near-inertial signal. Comparing the down-sampled data from 2017 to 2018 with a near-inertial bandpass applied to the original 3 hr data suggests that the effects of this aliasing are relatively mild, with agreement to within 10% of both energy and shear between the bandpass and downsampled cases, and do not impact the conclusions of this study. The near-inertial signal also potentially contains tidal velocities, as the mooring location is just below the critical latitude for the M2 tides. Tides are weak at this location but inseperable from near-inertial internal waves in this data set.

4. Results

4.1. Year-to-Year and Seasonal Variability

4.1.1. Sea Ice

The overall decline of Arctic sea ice is well-documented, and changes in ice cover are locally apparent at BGOS mooring A over the course of the BGOS program (Figures 3 and 5a). Prior to 2007 sea ice concentrations were consistently above 90%, while in the 11 years with data since 2007, there were only three summers in which there was no open water. In 2005, ice concentration was over 99% every day of the year, while in 2016 there were 88 days with ice concentration less than 70%. The increase in days with partial sea ice cover has been driven by a combination of longer periods of melt and freeze in the spring and fall and by more frequent winter leads, which rarely occurred at mooring A prior to 2008. Sea ice concentration had a bimodal distribution, with complete ice cover or ice free conditions that were more common than intermediate states. The overall trend in annual sea ice concentration over the mooring deployment (only considering 12 months periods over which we have ≥80% complete data records) was −1% per year, reflecting both lengthening ice-free summers and an increase in days with partial ice cover.

Changes in ice draft were consistent with these observations (see also Krishfield et al. (2014)). Winter ice thinned, with a decline in days with ice thicker than 2 m from a peak of 116 days in 2007 to a minimum of 5 days in 2009, 2013, and 2017. Mean annual ice drafts ranged from 1.7 m in 2007 to 0.8 m in 2016. Annual mean ice draft had an overall trend of -4 cm year^{-1}, or a 60 cm reduction over the 15 years of this study.

Both ice concentration and draft exhibit a strong seasonal modulation, with the thickest ice found in May and June, and a minimum (in both draft and concentration) in September (Figures 3, 6a and 6b). Prior to 2007, sea ice cover was consistently present year-round at the mooring, so that 2007 marks the beginning of a transition in which the ice cover at mooring A completely vanishes in some years (Figure 3). The seasonal cycle in ice concentration was much more pronounced from 2007 onwards (Figure 6a). In contrast, the seasonal cycle in draft has a similar amplitude in the period from 2003 to 2006 and 2007–2018, although the mean draft has declined.

Sea ice concentration observed locally at the mooring was generally quite similar to satellite observations at 3 km scales at this location, except in 2015 when the satellite saw less ice cover (Figure 3a).

4.1.2. Near-Inertial Energy and Stratification

The mooring record from 2003 to 2018 shows sizable year-to-year variability in near-inertial energy at depths from 100 to 300 m (Figures 4a and 5d). The mean near-inertial energy over this period was 3.6×10^{-4} m^2 s^{-2} (standard deviation 1.5×10^{-4} m^2 s^{-2}) with no statistically significant trend in annually averaged near-inertial energy.

Internal wave energy is affected by stratification in a WKB sense (Leaman & Sanford, 1975). Stratification (N^2) at depths of 100–300 m showed less year-to-year variability than other quantities, with a depth mean $N^2 = 9.9 \times 10^{-5}$ rad^2 s^{-2} and standard deviation of 7.4×10^{-6} rad^2 s^{-2} (Figures 4c and 5c). Stratification had an interannual trend of 1.5×10^{-6} rad^2 s^{-2}, consistent with other studies that have observed increasing stratification in the western Arctic due to increased freshwater inputs and the intensification of the Beaufort Gyre (Proshutinsky et al., 2019). The depth span of this analysis is beneath the deepest winter mixed layers, minimizing variability.

Near-inertial energy had a clear seasonal modulation, with highest values in the summer months of August and September, consistent with energy being maximized when ice concentration is low (Figures 4a and 6c). This

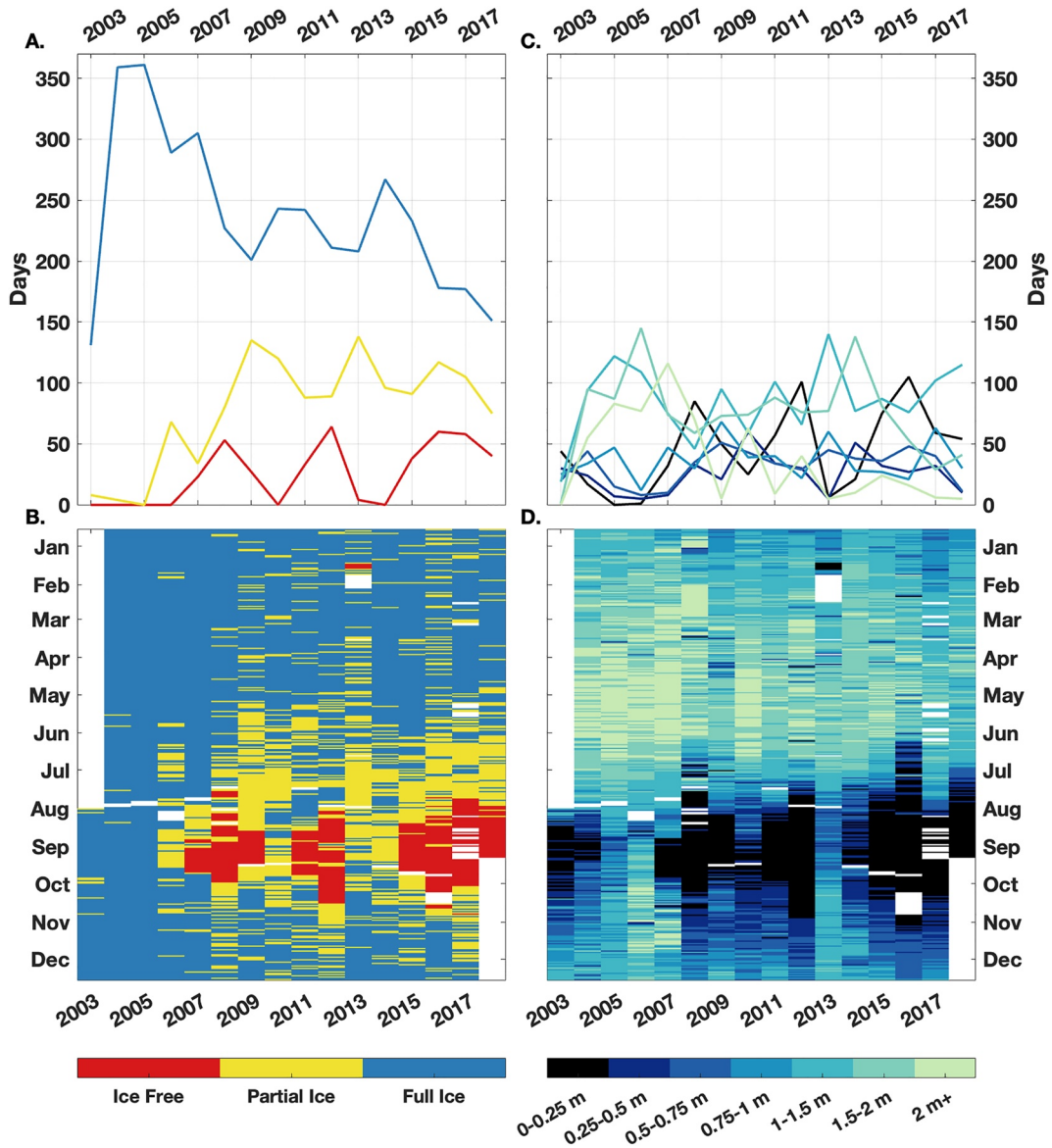

Figure 3. Ice conditions during 2003–2018. (a) Number of days with ice free (red), partial ice cover (yellow), and full ice cover (blue) conditions for each year (note that 2003 and 2018 were incompletely sampled). (b) Daily ice concentration for each month (*y*-axis) and year (*x*-axis), colored by ice conditions as in panel (a). (c) Number of days for each year in which ice draft was within the given ranges. (d) Daily ice draft for each month (*y*-axis) and year (*x*-axis).

seasonal cycle had slightly larger amplitude and a narrower summer peak in 2003–2006 compared to the later part of the record, suggesting that longer melt and freeze periods in ice cover impact mean energy. No significant seasonal cycle was observed in stratification.

4.1.3. Shear and Mixing

Near-inertial shear, R_ω, and ϵ_{IW} showed high variability over the mooring record (Figures 4b, 4d, 4e and 5e–5g). Mean near-inertial shear from 100 to 300 m was 3.8×10^{-5} s^{-1} (standard deviation 2.8×10^{-5} s^{-1}). Mean R_ω was 14 (standard deviation 13) and mean ϵ_{IW} was 4.7×10^{-10} W kg^{-1} (standard deviation 4.9×10^{-10} W kg^{-1}). This mean ϵ_{IW} is consistent with microstructure studies in the region; for instance Rippeth et al. (2015) found mean ϵ values from 5×10^{-10} to 2×10^{-9} W kg^{-1} in the central Arctic. Inferred values of ϵ_{IW} spanned 4 orders of magnitude, with a minimum of 3.6×10^{-12} W kg^{-1} and a maximum of 2.2×10^{-8} W kg^{-1}. The mean R_ω was higher

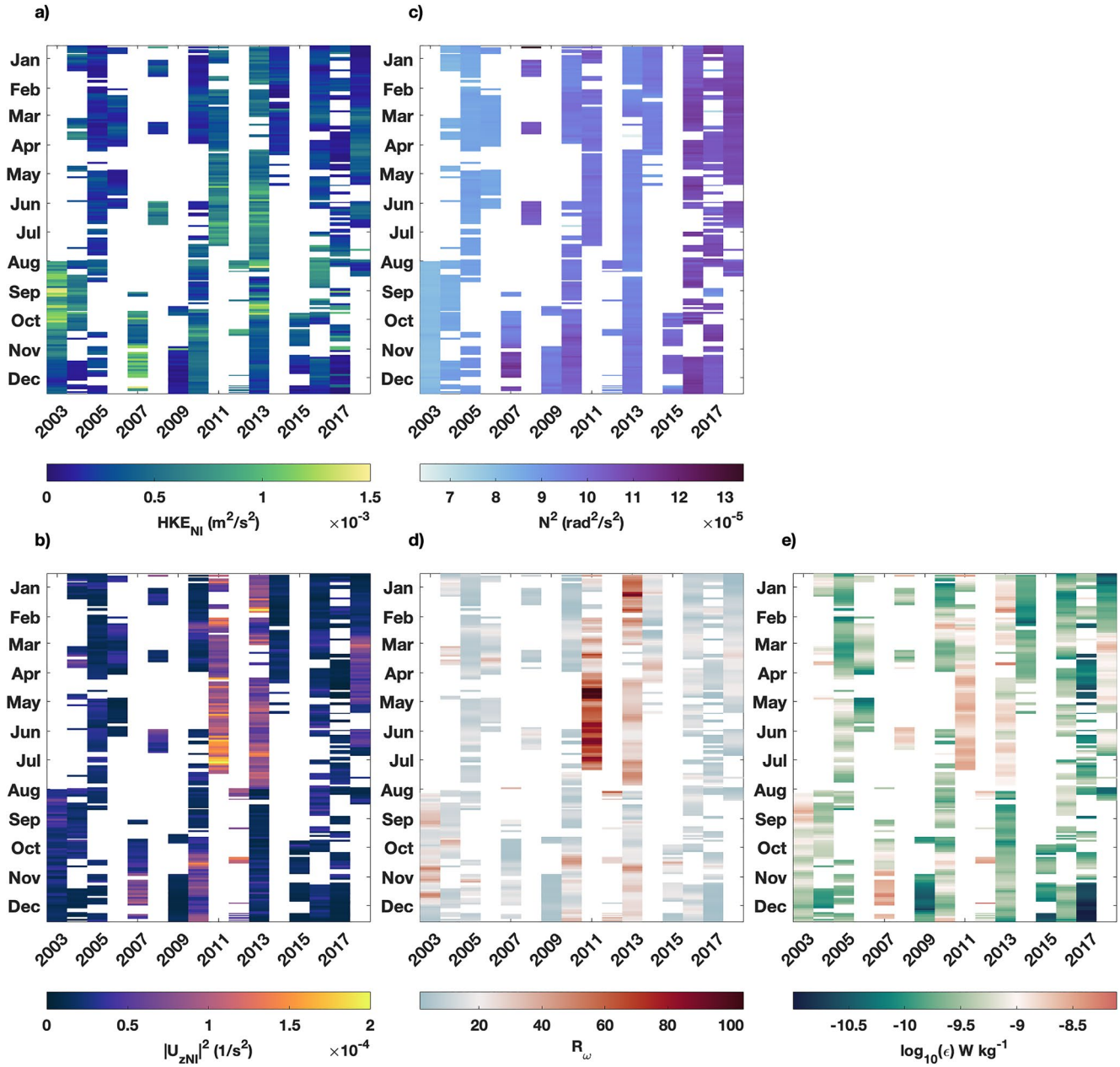

Figure 4. Daily ocean conditions from 100 to 300 m depth for all profiles included in this study, with months on the *y*-axis and years on the *x*-axis: (a) NI HKE, (b) NI Shear, (c) N^2, (d) R_ω, and (e) ϵ_{IW} from the finescale parameterization.

than the values often assumed for the finescale parameterization (usually 7 or 11 (Dosser et al., 2021; Guthrie et al., 2013)). There was no statistically significant trend in near-inertial shear, R_ω, or ϵ_{IW}.

Near-inertial shear, R_ω, and ϵ_{IW} did not show seasonal cycles at the analysis depths, suggesting that the observed variability was due to intermittent processes that occurred throughout the year (Figures 4b, 4d, 4e and 6d–6f). A slight seasonal cycle is perhaps more apparent in shear in the 2007–2018 period, with elevated winter shear, but this signal is small. In the years from 2003 to 2006, ϵ_{IW} tended to decline in October through December, but this behavior was not present in other years.

In summary, sea ice concentration and draft both declined over the mooring record. There was no significant inter-annual trend in near-inertial energy, near-inertial shear, R_ω or ϵ_{IW}. The seasonal cycles of sea ice concentration,

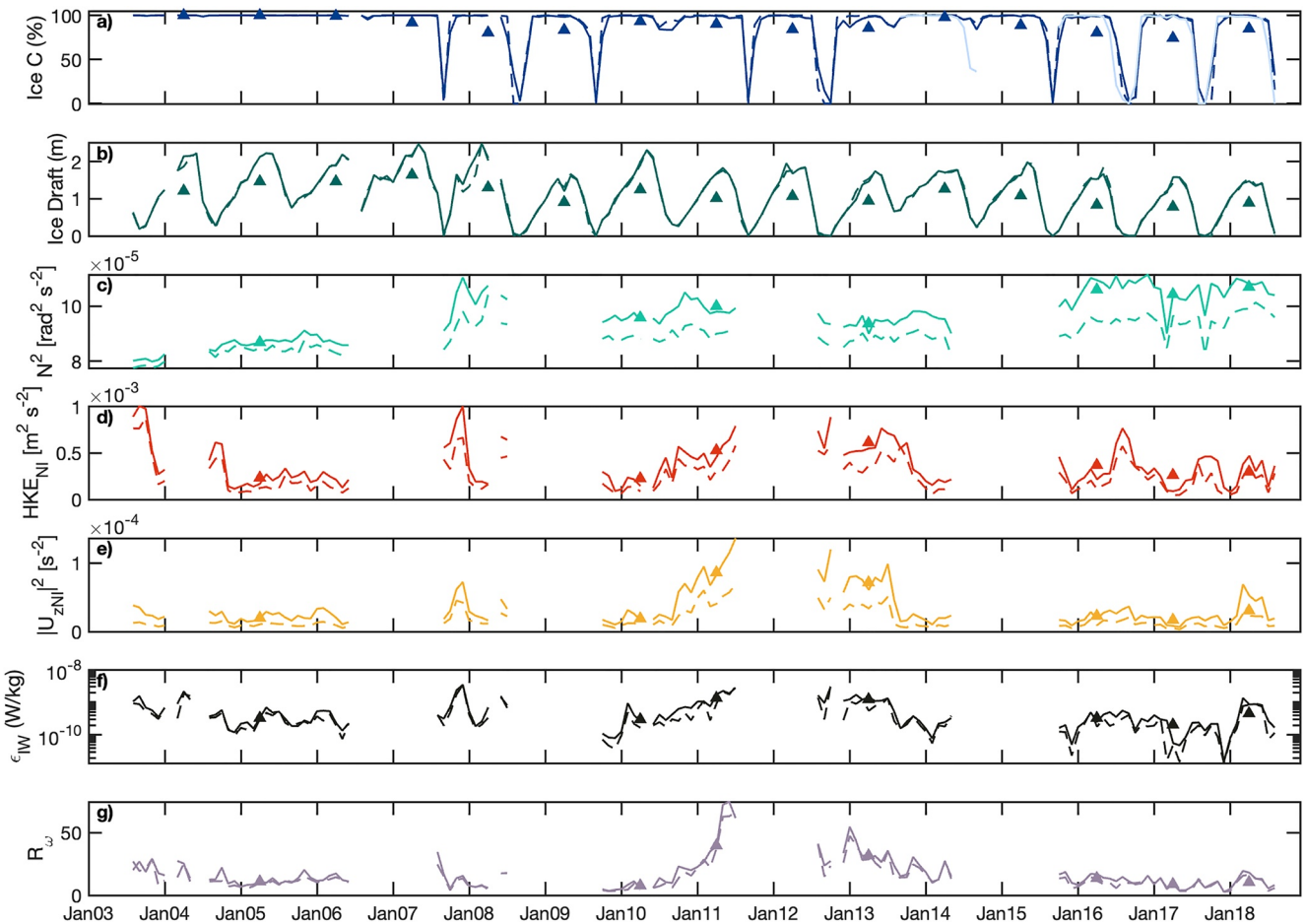

Figure 5. Monthly mean values for months with at least six profiles of (a) daily ice concentration, (b) ice draft, (c) N^2, (d) near-inertial energy, (e) near-inertial shear, (f) ϵ_{IW}, and (g) R_ω. Means are shown as solid lines, with medians dashed. For 12 month periods in which at least 11 months of data are available, annual averages are shown as solid triangles. All oceanic quantities are shown for depths 100–300 m (100 m was chosen as the upper limit to keep comparisons consistent across years).

ice draft, and near-inertial energy were consistent with the hypothesis that energy is maximized when sea ice is reduced.

4.2. Vertical Wavenumber Spectra by Ice Conditions

Vertical wavenumber spectra indicate that spectral energy was up to an order of magnitude lower than the Garrett-Munk prescription (Figures 7a and 7b). Shear spectral density peaked at wavenumbers of 3.9×10^{-2} cpm. The low observed energy at small vertical wavenumbers is consistent with prior observations in the region (Fine et al., 2021; Guthrie et al., 2013; Levine & Paulson, 1985; Morison et al., 1985). To assess how changes in sea ice conditions influenced energy in the internal wavefield, observations were binned based on local ice concentration, as described in Methods (3.1). Differences in the vertical wavenumber spectra associated with these different conditions are first considered (Figures 7a–7c). At low wavenumbers ($k_z < 5 \times 10^{-3}$ cpm) ice-free conditions were more energetic than other conditions. At high wavenumbers ($k_z > 2 \times 10^{-2}$ cpm), both partial and ice-free conditions had slightly more energy than full ice cover. However, in the wavenumber range 7×10^{-3} cpm $< k < 2 \times 10^{-2}$ cpm, differences between the ice conditions were almost negligible, with ice free conditions associated with slightly less energy than either partial or complete ice cover. Mean velocity $|\langle U_{WKB} \rangle|^2$ was greatest for ice free conditions (6.4×10^{-4} m^2 s^{-2}), and was lower for partial (4.7×10^{-4}m^2 s^{-2}) and full (4.4×10^{-4} m^2 s^{-2}) ice cover. Mean shear $|\langle U_{zWKB} \rangle|^2$ was higher for partial ice cover and ice free conditions (1.1×10^{-5} s^{-2} and 1.2×10^{-5} s^{-2}, respectively) but lower for full ice cover (8.6×10^{-6} s^{-2}). This spectral view demonstrates that

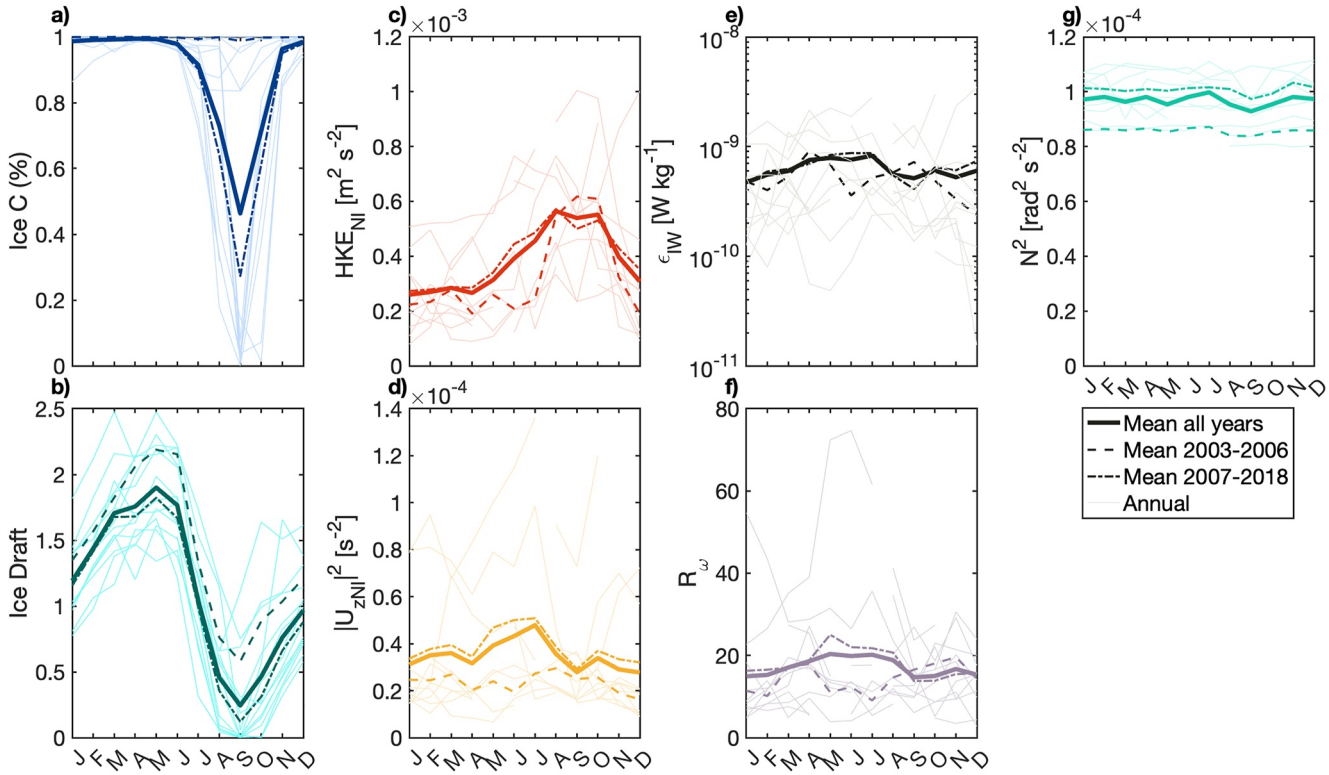

Figure 6. Seasonal cycle by month for (a) ice concentration, (b) draft, (c) near-inertial energy, (d) near-inertial shear, (e) ϵ_{IW}, (f) R_{ω}, and (g) N^2. Light curves show yearly data. Dashed lines show monthly averages from 2003 to 2006, and dash-dotted lines show monthly averages from 2007 to 2018. All oceanic quantities are shown for depths 100–300 m.

the vertical scales of the internal wavefield do not vary uniformly across ice conditions, with implications for the relationship between sea ice cover and vertical mixing.

Assuming internal wave energy primarily enters the ocean due to wind forcing at the surface, the ratio of downwards to upwards energy propagation under different ice conditions provides an indication of how varying ice conditions impact the forcing of the internal wavefield. In general downward propagation exceeded upward propagation at low wavenumbers, consistent with the premise that most energy enters the internal wavefield at large vertical scales due to surface forcing. The ratio between downward and upward propagation was largest for ice-free conditions. At intermediate wavenumbers, downward propagation was strongest for partial ice cover conditions (Figure 7c). At high wavenumbers, the ratio was noisy and declined to near 1, suggesting that the internal wavefield at these scales, and the vertical mixing that results, were derived from older waves that may have refracted, reflected, or otherwise interacted with other waves and flows enough to be nearly random in direction.

For days with full ice cover (ice concentration >99%), binning data by daily ice draft revealed an analogous relationship between ice draft and the internal wavefield (Figures 7d–7f). Here, 0.75 m is taken to differentiate "thick" and "thin" ice conditions (the qualitative relationship is not sensitive to the choice of cutoff). At wavenumbers $k_z < 2 \times 10^{-2}$ cpm, velocity and shear spectra were elevated for thin ice conditions relative to thick ice. In this wavenumber range, the average ratio of downward propagating energy was greater than one for both thin and thick ice, but was higher for thin ice. Mean velocity $|\langle U_{WKB} \rangle|^2$ was higher for thin ice (5.7×10^{-4} m^2 s^{-2}), and lower for thick ice (4.1×10^{-4} m^2 s^{-2}). Conversely, mean shear $|\langle U_{zWKB} \rangle|^2$ was identical for thick and thin ice (8.6×10^{-6} s^{-2}).

The central point from this analysis is that mean near-inertial velocity depends more strongly on both ice cover and ice thickness under full ice cover, relative to mean near-inertial shear. The differing behavior of velocity and shear appears contradictory but can be understood with reference to the vertical wavenumber spectra. The velocity spectra were red, with spectral power highest at low vertical wavenumbers. Shear spectra were much whiter, as shear is the vertical derivative of velocity, with a peak in the wavenumber range from 2×10^{-2} to 6×10^{-2} cpm.

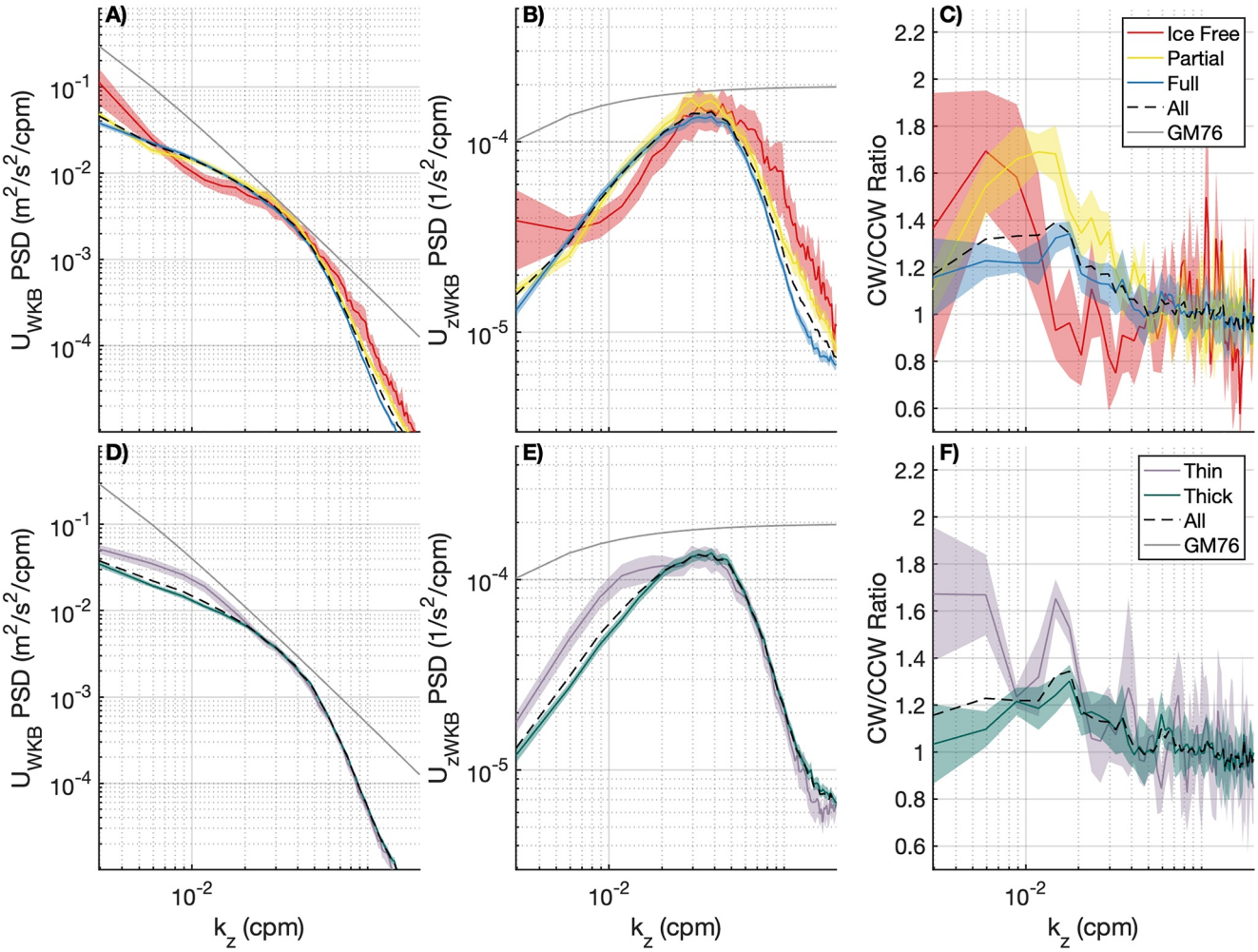

Figure 7. Spectral analysis of Wentzel-Kramers-Brillouin stretched and scaled velocity and shear data from 100 to 300 m depth binned by (a–c) ice concentration and (d–e) ice draft. (a) Velocity spectra; (b) shear spectra; (c) ratio of downwards to upwards propagation for ice free (red, daily ice concentration under 5%), partial ice cover (yellow, daily ice concentration between 5% and 99%), and full ice cover (blue, ice concentration >99%). The dashed line indicates the mean of each quantity over all data. (d) Velocity spectra; (e) shear spectra; (f) ratio of downwards to upwards propagation for thick ice (ice draft >0.75 m) and thin ice (ice draft <0.75 m) during days with >99% ice concentration. Light gray lines in panels (a, b, d and e) indicate the Garrett-Munk 76 spectra (Cairns & Williams, 1976; Garrett & Munk, 1972, 1975). Shaded areas define 95% confidence intervals. The vertical wavenumber k_z corresponds to stretched depths.

When we bin spectra by ice conditions, we see that times of both no ice cover and thin ice had more power in the low-wave number band, which manifests in larger mean velocity for these conditions. However, at the higher wavenumbers that largely determine mean shear, there was very little sensitivity to sea ice concentration or draft.

The ratio of downwards to upwards propagating internal waves also suggests a mechanism for why ice-free conditions and thin ice were both associated with increased energy but not increased shear. In ice-free conditions, this ratio was higher at low wavenumbers than for either partial or full ice cover, indicating that more energy is put into motions with large vertical scales in ice-free conditions. A similar effect occurs for thin ice relative to thick ice, with an elevated ratio of downwards to upwards propagation suggesting that there is more energy at these larger vertical scales when ice is thin. However, for the intermediate wavenumber range (around the shear peak scale of 2–6 $\times$ 10^{-2} cpm) the ratio of upwards to downwards propagation was lower for ice free conditions than for either partial or full ice cover, suggesting that less energy was put into intermediate scales under ice-free conditions. Similarly, ratios of upwards and downwards propagation were nearly identical between thick and thin ice conditions in this wavenumber range. Thus while increased energy enters the ocean when there is no ice or thin ice, this energy is largely concentrated in low-wavenumber waves, which are associated with relatively weak shear variance.

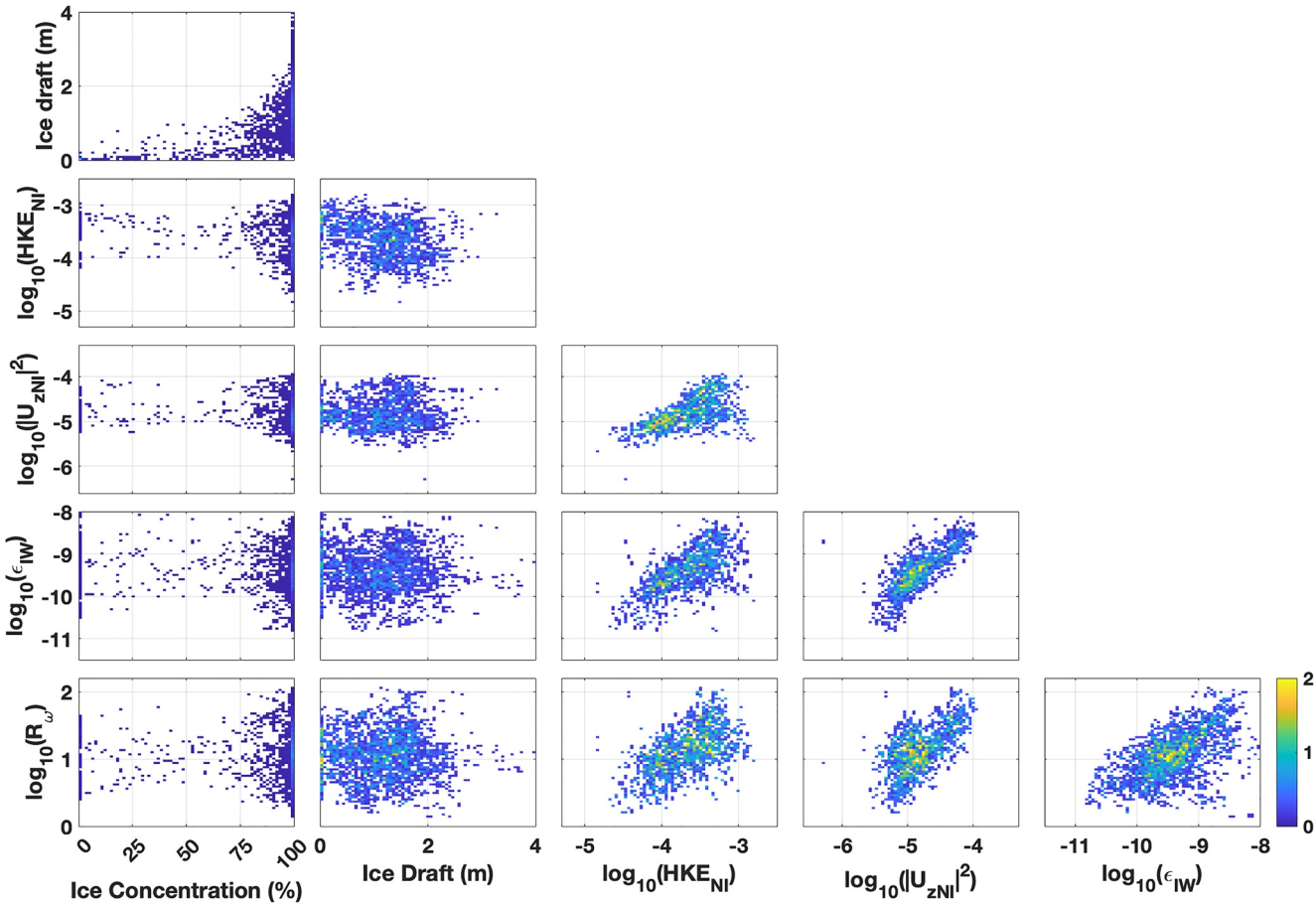

Figure 8. Joint probability density functions between ice concentration, ice draft, NI energy, NI shear, ϵ_{IW}, and R_ω. Median NI energy and shear are calculated between 50 and 300 m, while median ϵ_{IW} and R_ω are calculated from 75 to 300 m. Ice concentration (far left) has a bimodal distribution complicating interpretation of the relationship.

Table 4
Correlations Between Ice Concentration (Ice C, %), Ice Draft (Ice D, m), Near-Inertial Horizontal Kinetic Energy ($log_{10}(HKE_{NI})$ [$m^2\ s^{-2}$]), Near-Inertial Shear ($log_{10}(|U_{zNI}|^2)$ [s^{-2}]), the Finescale Turbulent Dissipation Rate ($log_{10}(\epsilon_{IW})$ ($W\ kg^{-1}$)), and the Finescale Shear-to-Strain Ratio (R_ω)

	Ice C	Ice D	$\log_{10}(HKE_{NI})$	$\log_{10}(\lvert U_{zNI}\rvert^2)$	$\log_{10}(\epsilon_{IW})$
Ice D	0.55[a]	–	–	–	–
$\log_{10}(HKE_{NI})$	−0.18[a]	−0.32	–	–	–
$\log_{10}(\lvert U_{zNI}\rvert^2)$	−0.04[a]	0.03	0.60	–	–
$\log_{10}(\epsilon_{IW})$	−0.05[a]	−0.02	0.64	0.79	–
$\log_{10}(R_\omega)$	0.03[a]	0.005	0.54	0.62	0.56

[a]Note that ice concentration is bimodally distributed, complicating interpretation of these correlations.

4.3. Relationships Between Ice, Internal Waves, and Mixing

To quantify the relationships between ice concentration, ice draft, near-inertial energy, near-inertial shear, R_ω, and ϵ_{IW}, we begin by examining overall correlations (Figure 8, Table 4). For oceanic quantities we consider the median value of each profile between depths of 50–300 m, except for ϵ_{IW} and R_ω in which the median between depths of 75–300 m was used.

We find that near-inertial energy and shear were correlated, and that both of these were correlated with ϵ_{IW} and R_ω. These relationships are consistent with the notion of downscale energy transfer, so that energy input even at relatively large vertical scales (as would be associated with near-inertial internal waves) is correlated with microscale dissipation. (Note that the finescale parameterization assumes a relationship between finescale shear and microstructure dissipation, so this correlation is built into the parameterization.) The correlation between R_ω and near-inertial shear and energy was also expected, as near-inertial waves have much larger horizontal than vertical velocities so that near-inertial shear variance is greater than the corresponding near-inertial strain variance.

Ice draft and near-inertial energy were negatively and approximately linearly correlated, with thicker ice associated with less near-inertial energy

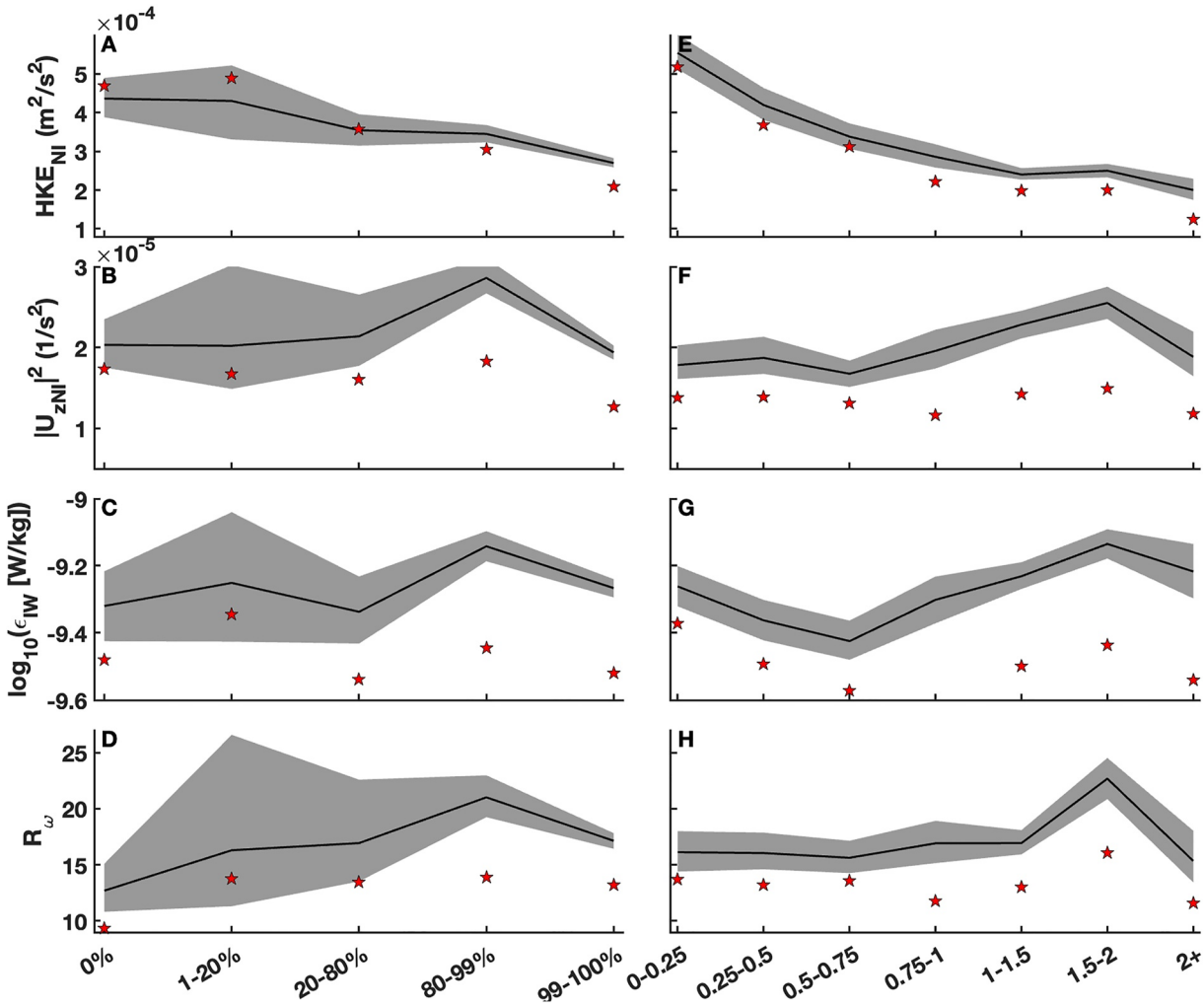

Figure 9. Binned means (lines) and medians (stars) by (a–d) ice concentration and (e–h) ice draft of (a and e) NI energy, (b and f) NI shear, (c and g) $\log_{10}(\epsilon_{IW})$, and (d and h) R_ω. Depth ranges of 50–300 m were considered for NI energy and shear, while ϵ_{IW} and R_ω were calculated from 75 to 300 m. The shaded regions show 95% bootstrapped confidence intervals for the mean values. The mean of ϵ_{IW} was calculated as the arithmetic mean.

independent of ice concentration. This is consistent with the observed seasonal cycles in ice draft and with the hypothesis that thicker sea ice shields the ocean from wind forcing.

Ice concentration was positively correlated with ice draft, and negatively correlated with near-inertial energy. However, ice concentration is unique in that it was bimodally distributed. Full ice cover occurs much more frequently than other conditions, skewing the distribution. Interpretation of the direct correlation between ice concentration and oceanic conditions is thus complicated.

We next bin data by ice concentration and draft to examine their effect on near-inertial energy, near-inertial shear, and ϵ_{IW}. By only considering mean and median values, a relatively fine partitioning with ice concentration and draft is possible. Considering mean quantities within each of 5 bins based on ice concentration, near-inertial energy tended to decrease with increasing ice concentration (Figure 9a). This relationship is consistent with the hypothesis that ice cover inhibits the transfer of wind momentum into near-inertial internal waves. Near-inertial shear did not follow the same pattern. Instead, near-inertial shear was nearly constant with increasing ice concentration, and attained its maximum in ice conditions with 80%–99% ice concentration. Mean values of ϵ also reached a maximum in ice concentrations of 80%–99%, although the dependence of ϵ_{IW} on ice concentrations was very weak. Mean R_ω generally mirrored near-inertial shear, but was relatively low for ice-free conditions and

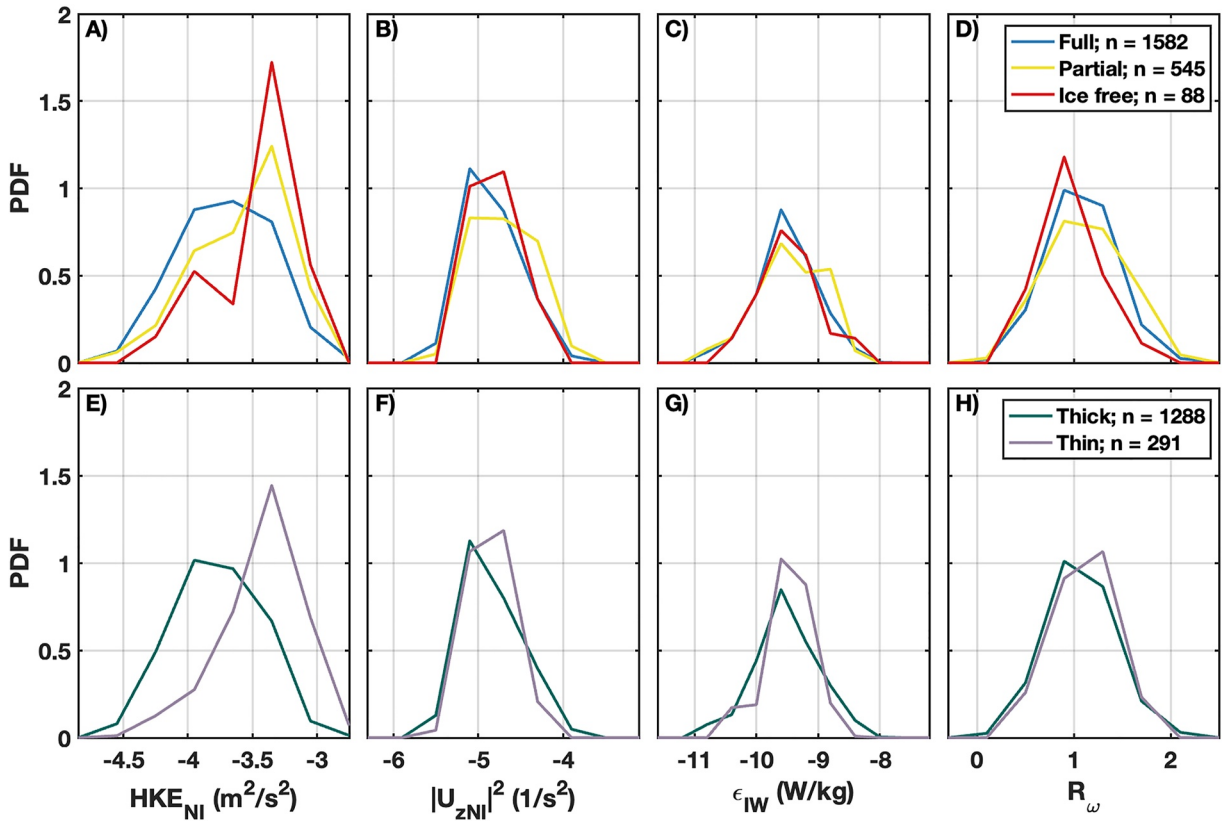

Figure 10. Probability density functions of oceanic quantities, with data binned by (a–d) daily ice concentration and (e–h) ice draft. Full, partial, and ice free conditions as well as thick and thin ice as in Figure 7. Near-inertial energy and shear are given as daily median values in the 50–300 m depth range, while ϵ_{IW} and R_ω are medians over 75–300 m. Panels (a and e) show near-inertial energy, (b and f) near-inertial shear, (c and g) ϵ_{IW}, and (d and h) R_ω.

varied significantly in 1%–20% ice cover. Generally, trends were similar for ice draft, with a decline in near-inertial energy associated with increasing ice draft, but no associated decline in near-inertial shear, ϵ_{IW}, or R_ω.

The medians of near-inertial energy and shear, R_ω, and ϵ_{IW} binned by ice concentration and ice draft are different from their means. Except for near-inertial energy, medians are uniformly lower than the mean, indicating that mean values were dominated by rare but powerful events, typical of a lognormal distribution. This effect holds whether values are binned based on ice concentration or ice draft. We choose to focus our analysis on mean quantities rather than median, as vertical heat transport scales linearly with turbulent dissipation, and thus the arithmetic mean better represents the impact these quantities have at a climatic scale. Large confidence intervals indicate significant variance in the data, particularly in ice free and partial-ice cover conditions, which were rare relative to full ice cover.

We next examine probability density functions (PDFs) of near-inertial energy, near-inertial shear, R_ω, and ϵ_{IW} binned by ice concentration and ice draft (Figure 10). For this analysis, daily median values of each quantity are taken over the 50–300 m depth range, except for ϵ_{IW} and R_ω in which medians are calculated over the 75–300 m depth range. Probability density functions of near-inertial energy under different ice concentrations indicate that the differences between the mean values in ice covered and ice-free conditions were robust (Figures 9 and 10a–10d). Near-inertial energy was approximately lognormally distributed, and the peak of this distribution was higher when less ice cover was present. However, near-inertial shear, R_ω, and ϵ_{IW} did not show this effect to nearly the same degree. Near-inertial shear in full ice cover was slightly lower than in other conditions, but this effect was small, and the distributions of near-inertial shear in ice free and partially ice covered conditions were not statistically distinct. The highest values of near-inertial shear were associated with partial ice cover. Similarly, PDFs for full ice cover show separation based on ice thickness. The distribution of near-inertial energy was higher for thin ice conditions, but this separation was not apparent for near-inertial shear, ϵ_{IW}, or R_ω.

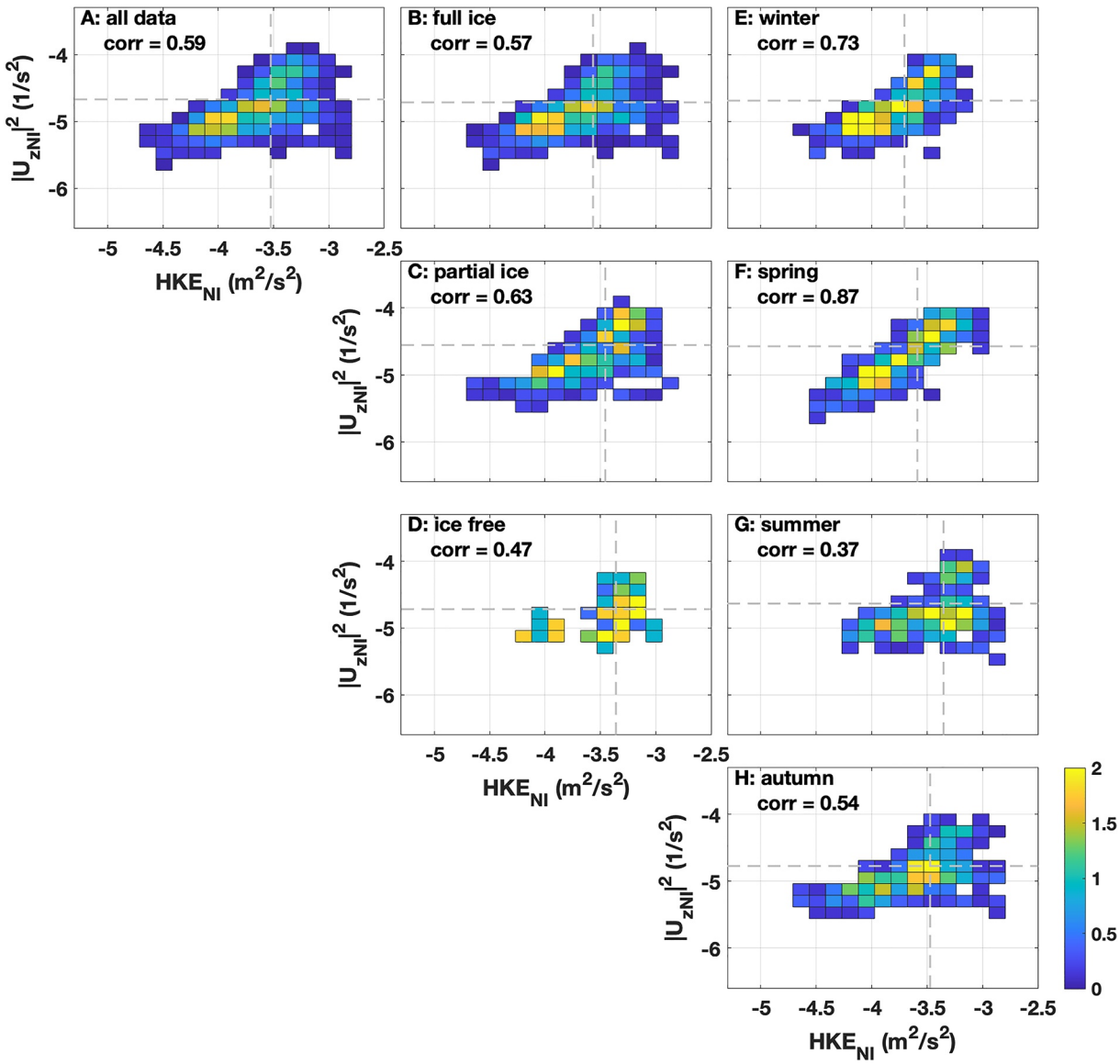

Figure 11. Joint probability density functions of near-inertial energy and shear, binned for (a) all data, (b) full ice cover (concentration >99%), (c) partial ice cover (5% < concentration <99%), (d) ice free conditions (concentration <5%), (e) winter (JFM), (f) spring (AMJ), (g) summer (JAS), and (h) autumn (OND). Average values of near-inertial energy and near-inertial shear for each data subset are indicated by dashed gray lines in each panel. Near-inertial energy and shear are given over 50–300 m, while ϵ_{IW} and R_ω are given over 75–300 m.

4.4. The Effect of Ice Concentration on the Relationship Between Energy and Shear

Previously we observed that near-inertial energy and near-inertial shear were correlated, as is expected due to the physical relationship between these quantities (Figure 8). However, there were differences in the relationship between near-inertial energy and near-inertial shear for different ice conditions. The correlation between energy and shear was weaker in ice-free conditions than in either partial or total ice cover (Figures 11b–11d). There was also a seasonal dependence of the correlation, with energy and shear most correlated in the spring (Figures 11e–11h). Correlation declined sharply in the summer, then increased in the autumn and winter. Splitting by season, rather than ice cover, produced the largest correlations between energy and shear (found in winter and spring). This suggests that factors beyond local ice cover at the mooring influenced this correlation. Energy that was input at large vertical scales in summer may have taken several months to dissipate, so that the correlation remained weak until the following winter. Remote changes in ice cover also possibly impacted the internal

wavefield such that even during ice-covered summer and fall conditions the correlation was weaker due to remote forcing.

Taken together, the observed patterns cast doubt on aspects of the hypothesized wind-ice-ocean feedback loop described in the introduction. In the first step of the feedback loop, decreased ice cover is expected to increase near-inertial energy into the upper ocean. The observed relationship between ice concentration and near-inertial energy is consistent with this hypothesis. However, the second step of the feedback loop requires that this increased energy in ice-free conditions is associated with increased small-scale shear and turbulent dissipation. Here, we find that both near-inertial shear and ϵ_{IW} vary independently of ice concentration and draft. This is true even assuming there is a lag between ice cover and near-inertial shear and ϵ_{IW}, that is, lagging ice cover by 1–3 months does not improve the correlation between shear and ice concentration or ϵ_{IW} and ice concentration.

5. Discussion

5.1. Summary and Limitations

Analysis of a single 15-year timeseries encompassing a variety of ice conditions has lead to four main conclusions about the upper 50–300 m of the Arctic Ocean:

1. Decreasing sea ice concentration and draft increase near-inertial energy on seasonal (Figure 6) and daily timescales (Figures 8 and 10).
2. Decreasing sea ice concentration and draft do not directly increase near-inertial shear or inferred turbulence, contrary to the wind-ice-ocean feedback hypothesis (Figures 9 and 10).
3. Local ice conditions determine the vertical scales at which near-inertial energy enters the ocean, with the increased energy in low ice draft and low ice concentration conditions input at low vertical wavenumbers that have relatively little high-wavenumber shear. This relationship explains why decreasing sea ice correlates with increased energy but not increased shear (Figure 7).
4. In spite of the different response of near-inertial energy and near-inertial shear to varied ice conditions, energy and shear are generally correlated in a variety of conditions. Their correlation evolved seasonally, with the strongest correlation in the spring and the weakest in the autumn (Figure 11).

The differing effects that sea ice conditions had on energy and ϵ_{IW} are explained by the vertical scales with which internal waves are generated, a key result of the present study. Ice free conditions were associated with more energetic internal waves of larger vertical scales, which are less susceptible to dissipation. The measurement time scales of near-inertial energy (taken over 6 hr) and ϵ_{IW} (windowed over 4 days to minimize spectral) are slightly different, which could arguably explain why ϵ_{IW} is less responsive to changes in ice draft and concentration than near-inertial energy is. However, near-inertial shear, which is measured on the same scales as energy, shows the same lack of dependence on ice conditions as ϵ_{IW}, and energy and ϵ_{IW} also respond differently to changes in ice conditions on seasonal and interannual times scales. We therefore conclude that the lack of correlation of shear and mixing with sea ice conditions is robust.

A key caveat is that the observed relationships are statistical. There is large variability in near-inertial energy, near-inertial shear, and ϵ_{IW} that cannot be linked to local sea ice conditions. The internal wavefield is forced by events that are episodic in nature, including local and farfield storms as well as sea ice rafting. Another inherent limitation of this study is the lack of oceanic measurements above 50 m depth. The BGOS moorings permit limited analysis above 50 m, and consequently we do not describe the mixed layer. Western Arctic mixed layers are highly seasonal, with summer ice melt creating a thin and very fresh mixed layer, with sharp stratification at its base separating it from halocline waters (Toole et al., 2010). Beginning in autumn and continuing through the winter, storms deepen the mixed layer, with typical maximum thickness in the spring of 40–50 m (Cole & Stadler, 2019). In the current study, we do not observe mixed layer depth, and thus cannot separate the influence of either mixed layer depth or the strength of stratification at the base of the mixed layer from changes in ice concentration and draft, which are also highly seasonal (Figure 6). It is possible that some of the relationships we observe between ice conditions and the internal wavefield are in fact mediated by mixed layer depth (e.g., Guthrie and Morison (2021)). However, the result that low sea ice concentration (which occurs in the late summer and early fall) is associated with relatively large vertical scales in the internal wavefield suggests that it is ice conditions rather than mixed layer depth that sets these vertical scales. Low ice concentration is associated with

a fresh and shallow summer mixed layer (Toole et al., 2010), which would be expected to force higher vertical wavenumbers if mixed layer depth primarily determined internal wave vertical scales.

A related limitation is the lack of estimates for ϵ_{IW} above 75 m. The 40–100 m depth range generally contains the temperature maximum associated with Pacific Summer Water (Timmermans et al., 2014). Stratification varies rapidly over this depth range so that the finescale parameterization is unlikely to perform well (Polzin et al., 2014). Assuming that ϵ_{IW} is relatively constant in depth as observed by Fine et al. (2021), average mixing rates in this depth range are unlikely to be large enough to support substantial heat fluxes (taking the buoyancy Reynolds number $Re_b = \epsilon/(\nu N^2)$, with $\epsilon = 5 \times 10^{-10}$ W kg^{-1}, $N^2 = 5 \times 10^{-4}$ rad^2 s^{-2} results in a buoyancy Reynolds number less than 1, suggesting molecular mixing in these conditions). However, more direct microstructure observations are needed to understand the importance of episodic mixing, including large near-inertial wave events and warm eddies that may be associated with larger vertical heat fluxes (Fine et al., 2018; Kawaguchi et al., 2012). The impacts of such events on oceanic vertical heat fluxes are poorly constrained by existing microstructure measurements.

5.2. Comparisons With Prior Studies

While the high year-to-year variability in ice concentration, near-inertial energy, near-inertial shear, and ϵ_{IW} combined with missing data in some years could undermine confidence in the observed year-to-year trends, the tendencies observed in this study are consistent with observations from a wide range of studies. Modest increases in Arctic internal wave energy have been observed as sea ice declines (Dosser & Rainville, 2016). On shorter timescales, near-inertial energy has been observed to increase in the absence of sea ice in the shelf seas (Martini et al., 2014; Rainville & Woodgate, 2009). Observations of ϵ_{IW}, on the other hand, suggest that ocean mixing is relatively insensitive to sea ice conditions, and that even when storms occur over open water the increase in ϵ in the upper ocean is modest (Dosser et al., 2021; Fine et al., 2021; Guthrie et al., 2013; Lincoln et al., 2016; Lique et al., 2014; Rippeth et al., 2017). Guthrie and Morison (2021) suggest that the high stratification and shallow summer mixed layers present in the Canada Basin limit vertical propagation of near-inertial energy even in the absence of sea ice. Here, we present an alternate explanation that the lack of increased mixing in the absence of sea ice is related to the vertical scales with which energy is input into the ocean. The observed increase in near-inertial energy at large vertical scales in ice free conditions relative to ice covered conditions (with generally deeper mixed layers) suggests that shallow summer mixed layers may not have a strong influence on internal wave generation.

Dosser et al. (2021) considered strain-based finescale parameterizations of ϵ_{IW} from all Arctic ITP data. In the Canada Basin, Dosser et al. (2021) found a geometric average ϵ_{IW} of 4.2×10^{-10} W kg^{-1} from 2002 to 2019, slightly lower than our interannual arithmetic average of ϵ_{IW} at mooring A of 4.7×10^{-10} W kg^{-1}. Dosser et al. (2021) found that while average dissipation rates are not increasing, ϵ_{IW} has a seasonal cycle which has become more pronounced since 2011, as ϵ_{IW} has increased in July and August and decreased in the winter months. This change in seasonal cycle is not apparent in the BGOS A data (Figures 4d and 6e), which could be related to differences in sampling between a fixed mooring and drifting ITP. The ITPs are embedded in a single piece of (usually multiyear) ice, and therefore tend to see a different range of ice conditions in a given year as they drift with the floe compared to the mooring, which observes varying ice conditions at a fixed location. The mooring observations suggest that in earlier years (2003–2006) ϵ_{IW} was relatively low from October through January. It is possible that the thinner (but not absent) ice in more recent years has led to elevated upper ocean mixing only in these months, as autumn storms have more access to open water.

5.3. Implications

One implication of this study is that variations in R_ω represent a potentially significant source of error for finescale parameterizations in the absence of velocity data (Dosser et al., 2021; Fine et al., 2021). How R_ω varies with strain and shear determines appropriate assumptions about the value of R_ω in the absence of concurrent velocity and CTD measurements (Chinn et al., 2016). In general R_ω increases with increasing shear, and decreases with increasing strain. In the current data set, we find the relationship between R_ω and shear is much stronger than its relationship with strain (Figure 12. The strain and shear in this figure are the quantities used in the finescale parameterization; see Section 3 for details). This is unfortunate in the context of the relatively high availability of

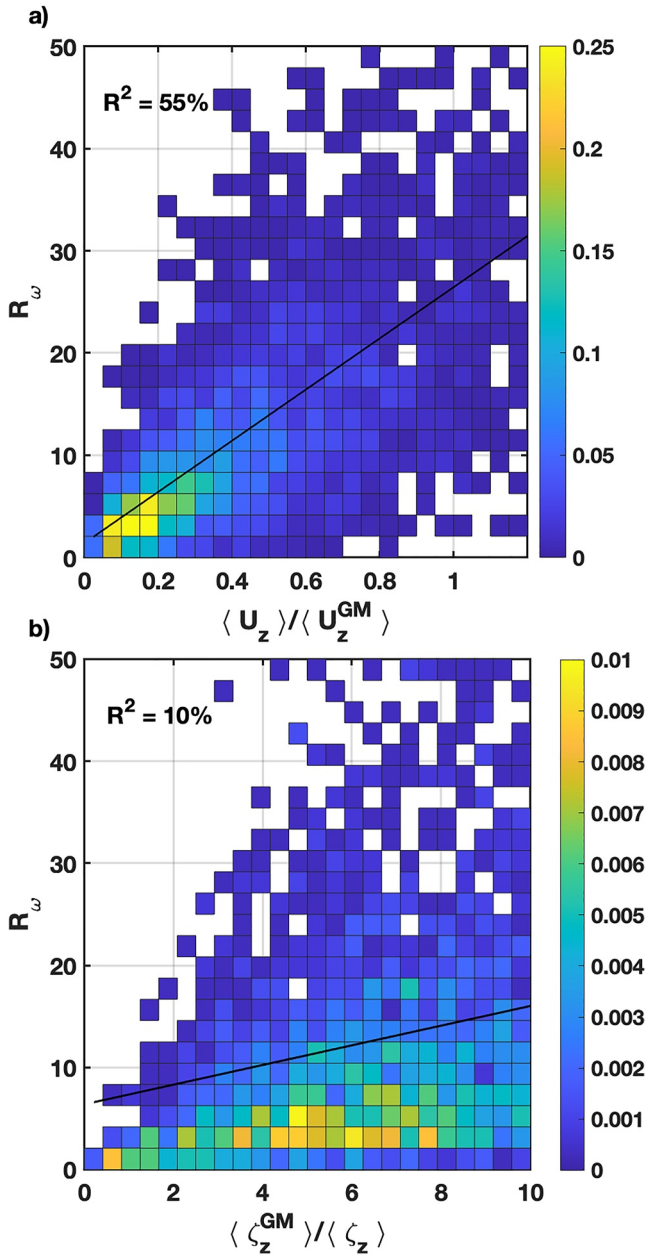

Figure 12. Joint probability density functions of all R_ω measurements over the entire data record with (a) normalized shear and (b) inverse normalized strain. The best fit slopes are in black.

Arctic CTD profiles without concurrent velocity observations. Strain alone only explains 10% of the variance in R_ω, while shear accounts for 55% of its variance. The results of this study additionally suggest that the seasonal variation of R_ω is small and that R_ω is uncorrelated with ice conditions. Thus bounding R_ω in the absence of colocated velocity and CTD data remains a challenge. However, the available measurements suggest that R_ω in the western Arctic tends to be larger than typically used values. The average value of R_ω observed in this study was 14, significantly higher than the average for the global (lower latitude) ocean of 7 calculated by Kunze et al. (2006).

This study presents a question of whether the excess energy input into the ocean in certain ice conditions dissipates slowly at undetectable levels, or in other regions of the ocean. Provided that the ocean is in steady state, this energy must eventually dissipate somewhere. The observed increases in energy are modest, and it is perhaps not surprising that this signal hasn't measurably impacted dissipation rates. The average near-inertial energy observed in full ice cover was 2.7×10^{-4} J kg^{-1}, while the average near-inertial energy observed in ice-free conditions was 4.4×10^{-4} J kg^{-1}. Assuming that the "excess" energy associated with ice-free conditions were to dissipate in the upper ocean within timescales on the order of a single ~12 hr inertial period, the corresponding increase in dissipation would be 4×10^{-9} W kg^{-1} (=1.7×10^{-4} J/kg/12 hr), just detectable above background dissipation. Conversely, following Gill (1984) and assuming the excess energy dissipates on timescales of 100 days, the dissipation increase would be only 2×10^{-11} W kg^{-1}, far below the sensitivity of microstructure measurements. The increased energy due to the decline in sea ice could thus slowly dissipate locally without leading to a detectable change in mixing rates. Arguably, even this small change in background dissipation could lead to higher background heat fluxes and impact to sea ice, thus closing the feedback loop, but this is a very small effect. Alternatively, the energy may also dissipate at different depths, or non-locally at topographic boundaries, or potentially when interacting with eddies. These mechanisms of dissipation contrast to observations in which near-inertial waves induced turbulent dissipation due directly to the shear associated with the near-inertial wavefield (e.g., Alford and Gregg (2001)). Our analysis suggests that the larger vertical scales associated with ice-free conditions result in minimal increases in shear, so that this type of near-inertial wave-driven local dissipation does not occur more frequently with sea ice decline.

An outstanding question raised by this study is why ice-free conditions tend to be associated with larger vertical scales. Throughout our analysis, we have assumed that the differing ratio of upwards and downwards propagation in depth under different seasons and ice conditions is a function of local generation. It is possible that differences in dissipation between seasons or ice conditions contribute to the observed characteristics of the internal wavefield. For example, it is not clear whether low mode internal waves are not generated to the same degree or are more rapidly dissipated in the presence of sea ice. Dissipation under ice cover has been shown to be significant, with slope and shelf observations consistent with a "one-bounce" hypothesis and dissipation under the sea ice cover (Pinkel, 2005). Unfortunately, the data set analyzed in this study is not ideal for investigating the extent to which the "one-bounce" hypothesis affects internal wave propagation in the open ocean away from topography. The relatively high wavenumber shear we consider is associated with slow enough vertical propagation speeds that most energy would be lost in the course of a single round trip journey to the ocean bottom. Thus the "one-bounce" hypothesis doesn't explain the relationships we see between sea ice conditions and the internal wavefield.

Alternatively, if the observed differences in vertical scales of shear are associated with wave generation rather than dissipation, this may indicate that the horizontal scales of forcing are different under ice-free conditions than in full ice cover. Gradients in these forcing scales in ice-free conditions occur at the edges of storms (Gill, 1984), whereas in ice-covered conditions inhomogeneities in the ice cover that mediates the transfer of wind into the ocean may play a bigger role. The results suggest these inhomogeneities could occur at smaller scales. Gradients in potential vorticity in the upper ocean also play a role in setting the horizontal scales of the internal wavefield, and the surface potential vorticity field may be influenced by the presence of sea ice (D'Asaro, 1995; Danioux et al., 2008; Manucharyan & Thompson, 2017). Further studies, particularly studies focusing on the horizontal variability of ocean, ice, and atmospheric conditions, are necessary to distinguish between these hypotheses.

A major conclusion of this study is that the decline in sea ice in the western Arctic is not currently leading to an increase in diapycnal mixing and resulting vertical heat fluxes that further accelerate ice decline. However, observations over the last 15 years do not necessarily constrain future conditions. The features of the western Arctic that keep mixing rates relatively low even in the absence of sea ice cover could themselves be modified in a climate with longer ice free seasons, larger areas of open water, warmer inflowing Pacific and Atlantic water, and bigger storms. While these observations do not indicate that a positive wind-ice-ocean feedback loop is operating in the western Arctic at present, in a rapidly changing climate current observations can only partially constrain future scenarios.

Data Availability Statement

Beaufort Gyre Observing System mooring data were collected and made available by the Beaufort Gyre Exploration Project based at the Woods Hole Oceanographic Institution (https://www.whoi.edu/beaufortgyre) in collaboration with researchers from Fisheries and Oceans Canada at the Institute of Ocean Sciences. Satellite data were processed and made available by the University of Bremen (Melsheimer & Spreen, 2019; Spreen et al., 2008) and accessed from https://seaice.uni-bremen.de/sea-ice-concentration/amsre-amsr2/ in March of 2020.

Acknowledgments
This work was supported by the Postdoctoral Scholar Program at Woods Hole Oceanographic Institution, with funding provided by the Weston Howland Jr. Postdoctoral Scholarship. S. T. Cole was supported by Office of Naval Research grant N00014-16-1-2381. The authors would like to thank John Toole for scientific conversations and insight, and all of those involved with the Beaufort Gyre Observing System program and Advanced Microwave Scanning Radiometer 2 for their work to collect these observations and make them available to the scientific community. The authors are additionally grateful to editor Laurie Padman and two anonymous reviewers for their insightful comments and suggestions on this work.

References

Aagaard, K., Coachman, L. K., & Carmack, E. (1981). On the halocline of the Arctic Ocean. *Deep-Sea Research Part A, Oceanographic Research Papers*, *28*(6), 529–545. https://doi.org/10.1016/0198-0149(81)90115-1

Alford, M. H., & Gregg, M. C. (2001). Near-inertial mixing: Modulation of shear, strain and microstructure at low latitude. *Journal of Geophysical Research*, *106*(C8), 16947–16968. https://doi.org/10.1029/2000JC000370

Armitage, T. W., Manucharyan, G. E., Petty, A. A., Kwok, R., & Thompson, A. F. (2020). Enhanced eddy activity in the Beaufort Gyre in response to sea ice loss. *Nature Communications*, *11*(1), 1–8. https://doi.org/10.1038/s41467-020-14449-z

Cairns, J. L., & Williams, G. O. (1976). Internal wave observations from a midwater float, 2. *Journal of Geophysical Research*, *81*(12), 1943–1950. https://doi.org/10.1029/jc081i012p01943

Carmack, E., Polyakov, I., Padman, L., Fer, I., Hunke, E., Hutchings, J., et al. (2015). Toward quantifying the increasing role of oceanic heat in sea ice loss in the new arctic. *Bulletin of the American Meteorological Society*, *96*(12), 2079–2105. https://doi.org/10.1175/BAMS-D-13-00177.1

Chanona, M., Waterman, S., & Gratton, Y. (2018). Variability of internal wave-driven mixing and stratification in Canadian Arctic shelf and shelf-slope waters. *Journal of Geophysical Research: Oceans*, *123*(12), 9178–9195. https://doi.org/10.1029/2018JC014342

Chinn, B. S., Girton, J. B., & Alford, M. H. (2016). The impact of observed variations in the shear-to-strain ratio of internal waves on inferred turbulent diffusivities. *Journal of Physical Oceanography*, *46*(11), 3299–3320. https://doi.org/10.1175/JPO-D-15-0161.1

Coachman, L. K., & Barnes, C. A. (1961). The contribution of Bering Sea water to the Arctic Ocean. *Arctic*, *14*(3), 147–161. Retrieved from http://www.jstor.org/stable/40506914

Cole, S. T., & Stadler, J. (2019). Deepening of the winter mixed layer in the Canada basin, Arctic Ocean Over 2006–2017. *Journal of Geophysical Research: Oceans*, *124*(7), 4618–4630. https://doi.org/10.1029/2019JC014940

Cole, S. T., Toole, J. M., Lele, R., Timmermans, M. L., Gallaher, S. G., Stanton, T. P., et al. (2017). Ice and ocean velocity in the Arctic marginal ice zone: Ice roughness and momentum transfer. *Elementa*, *5*. https://doi.org/10.1525/elementa.241

Cole, S. T., Toole, J. M., Rainville, L., & Lee, C. M. (2018). Internal waves in the Arctic: Influence of ice concentration, ice roughness, and surface layer stratification. *Journal of Geophysical Research: Oceans*, *123*(8), 5571–5586. https://doi.org/10.1029/2018JC014096

Danioux, E., Klein, P., & Rivièr, P. (2008). Propagation of wind energy in to the deep ocean through a fully turbulent mesoscale eddy field. *Journal of Physical Oceanography*, *38*(10), 2224–2241. https://doi.org/10.1175/2008JPO3821.1

D'Asaro, E. A. (1995). Upper-ocean inertial currents forced by a strong storm. Part III: Interaction of inertial currents and mesoscale eddies. *Journal of Physical Oceanography*, *25*, (11), 2953–2958. https://doi.org/10.1175/1520-0485(1995)025<2953:UOICFB>2.0.CO;2

Dosser, H. V., Chanona, M., Waterman, S., Shibley, N. C., & Timmermans, M. (2021). Changes in internal wave-driven mixing across the Arctic Ocean: Finescale estimates from an 18-year pan-Arctic record. *Geophysical Research Letters*, *48*(8), 1–10. https://doi.org/10.1029/2020gl091747

Dosser, H. V., & Rainville, L. (2016). Dynamics of the changing near-inertial internal wave field in the Arctic Ocean. *Journal of Physical Oceanography*, *46*(2), 395–415. https://doi.org/10.1175/JPO-D-15-0056.1

Fer, I. (2014). Near-inertial mixing in the central Arctic Ocean. *Journal of Physical Oceanography*, *44*(8), 2031–2049. https://doi.org/10.1175/JPO-D-13-0133.1

Fine, E. C., Alford, M. H., MacKinnon, J. A., & Mickett, J. B. (2021). Microstructure mixing observations and finescale parameterizations in the Beaufort Sea. *Journal of Physical Oceanography*, *51*(1), 19–35. https://doi.org/10.1175/JPO-D-19-0233.1

Fine, E. C., MacKinnon, J. A., Alford, M. H., & Mickett, J. B. (2018). Microstructure observations of turbulent heat fluxes in a warm-core Canada Basin eddy. *Journal of Physical Oceanography*, *48*(10), 2397–2418. https://doi.org/10.1175/JPO-D-18-0028.1

Garrett, C., & Munk, W. (1972). Space-time scales of internal waves. *Geophysical Fluid Dynamics*, *3*, 225–264. https://doi.org/10.1080/03091927208236082

Garrett, C., & Munk, W. (1975). Space-time scales of internal waves: A progress report. *Journal of Geophysical Research*, *80*(3), 291–297. https://doi.org/10.1029/jc080i003p00291

Ghaemsaidi, S. J., Dosser, H. V., Rainville, L., & Peacock, T. (2016). The impact of multiple layering on internal wave transmission. *Journal of Fluid Mechanics*, *789*, 617–629. https://doi.org/10.1017/jfm.2015.682

Gill, A. E. (1984). On the behavior of internal waves in the wakes of storms. *Journal of Physical Oceanography*, *14*(7), 1129–1151. https://doi.org/10.1175/1520-0485(1984)014<1129:otboiw>2.0.co;2

Gimbert, F., Jourdain, N. C., Marsan, D., Weiss, J., & Barnier, B. (2012). Recent mechanical weakening of the Arctic sea ice cover as revealed from larger inertial oscillations. *Journal of Geophysical Research*, *117*(5), 1–14. https://doi.org/10.1029/2011JC007633

Gonella, J. (1972). A rotary-component method for analysing meteorological and oceanographic vector time series. *Deep-Sea Research and Oceanographic Abstracts*, *19*(12), 833–846. https://doi.org/10.1016/0011-7471(72)90002-2

Gregg, M. C. (1989). Scaling turbulent dissipation in the thermocline. *Journal of Geophysical Research*, *94*(C7), 9686. https://doi.org/10.1029/jc094ic07p09686

Gregg, M. C., & Kunze, E. (1991). Shear and strain in Santa Monica basin. *Journal of Geophysical Research*, *96*(C9), 16709. https://doi.org/10.1029/91jc01385

Gregg, M. C., Sanford, T. B., & Winkel, D. P. (2003). Reduced mixing from the breaking of internal waves in equatorial waters. *Nature*, *422*(6931), 513–515. https://doi.org/10.1038/nature01507

Guthrie, J. D., & Morison, J. H. (2021). Not just sea ice: Other factors important to near-inertial wave generation in the Arctic Ocean. *Geophysical Research Letters*, *48*(3), 1–10. https://doi.org/10.1029/2020gl090508

Guthrie, J. D., Morison, J. H., & Fer, I. (2013). Revisiting internal waves and mixing in the Arctic Ocean. *Journal of Geophysical Research: Oceans*, *118*(8), 3966–3977. https://doi.org/10.1002/jgrc.20294

Jackson, J. M., Carmack, E. C., McLaughlin, F. A., Allen, S. E., & Ingram, R. G. (2010). Identification, characterization, and change of the near-surface temperature maximum in the Canada Basin, 1993–2008. *Journal of Geophysical Research*, *115*(5), 1–16. https://doi.org/10.1029/2009JC005265

Kawaguchi, Y., Itoh, M., & Nishino, S. (2012). Detailed survey of a large baroclinic eddy with extremely high temperatures in the Western Canada Basin. *Deep-Sea Research Part I Oceanographic Research Papers*, *66*, 90–102. https://doi.org/10.1016/j.dsr.2012.04.006

Kowalik, Z., & Proshutinsky, A. Y. (2013). The Arctic Ocean tides. In O. M. Johannessen, R. D. Muench, & J. E. Overland (Eds.), *Geophysical Monograph Series* (pp. 137–158).

Krishfield, R. A., Proshutinsky, A., Tateyama, K., Williams, W. J., Carmack, E. C., McLaughlin, F. A., & Timmermans, M.-L. (2014). Deterioration of perennial sea ice in the Beaufort Gyre from 2003 to 2012 and its impact on the oceanic freshwater cycle. *Journal of Geophysical Research: Oceans*, *119*(2), 1271–1305. https://doi.org/10.1002/2013JC008999

Kunze, E., Firing, E., Hummon, J. M., Chereskin, T. K., & Thurnherr, A. M. (2006). Global abyssal mixing inferred from lowered ADCP shear and CTD strain profiles. *Journal of Physical Oceanography*, *36*(8), 1553–1576. https://doi.org/10.1175/JPO2926.1

Leaman, K. D., & Sanford, T. B. (1975). Energy propagation of inertial waves. *Journal of Geophysical Research*, *80*(15), 1975–1978. https://doi.org/10.1029/jc080i015p01975

Lenn, Y. D., Rippeth, T. P., Old, C. P., Bacon, S., Polyakov, I., Ivanov, V., & Hölemann, J. (2011). Intermittent intense turbulent mixing under ice in the Laptev Sea continental shelf. *Journal of Physical Oceanography*, *41*(3), 531–547. https://doi.org/10.1175/2010JPO4425.1

Levine, M., & Paulson, C. (1985). Internal waves in the Arctic Ocean: Comparison with lower-latitude observations. *Journal of Physical Oceanography*, *15*(6), 800–809. https://doi.org/10.1175/1520-0485(1985)015<0800:iwitao>2.0.co;2

Lincoln, B. J., Rippeth, T. P., Lenn, Y.-D., Timmermans, M. L., Williams, W. J., & Bacon, S. (2016). Wind-driven mixing at intermediate depths in an ice-free Arctic Ocean. *Geophysical Research Letters*, *43*(18), 9749–9756. https://doi.org/10.1002/2016GL070454

Lique, C., Guthrie, J. D., Steele, M., Proshutinsky, A., Morison, J. H., & Krishfield, R. (2014). Diffusive vertical heat flux in the Canada Basin of the Arctic Ocean inferred from moored instruments. *Journal of Geophysical Research: Oceans*, *119*(1), 496–508. https://doi.org/10.1002/2013JC009346

Lu, P., Li, Z., Cheng, B., & Leppäranta, M. (2011). A parameterization of the ice-ocean drag coefficient. *Journal of Geophysical Research*, *116*(7), 1–14. https://doi.org/10.1029/2010JC006878

MacKinnon, J. A., Simmons, H. L., Hargrove, J., Thomson, J., Peacock, T., Alford, M. H., et al. (2021). A warm jet in a cold ocean. *Nature Communications*, *12*(1), 1–12. https://doi.org/10.1038/s41467-021-22505-5

Manucharyan, G. E., & Thompson, A. F. (2017). Submesoscale sea ice-ocean interactions in marginal ice zones. *Journal of Geophysical Research: Oceans*, *122*(12), 9455–9475. https://doi.org/10.1002/2017JC012895

Martin, T., Steele, M., & Zhang, J. (2014). Seasonality and long-term trend of Arctic Ocean surface stress in a model. *Journal of Geophysical Research: Oceans*, *119*(3), 1723–1738. https://doi.org/10.1002/2013JC009425

Martini, K. I., Simmons, H. L., Stoudt, C. A., & Hutchings, J. K. (2014). Near-inertial internal waves and sea ice in the Beaufort Sea. *Journal of Physical Oceanography*, *44*(8), 2212–2234. https://doi.org/10.1175/JPO-D-13-0160.1

McPhee, M. G. (2012). Advances in understanding ice-ocean stress during and since AIDJEX. *Cold Regions Science and Technology*, *76–77*, 24–36. https://doi.org/10.1016/j.coldregions.2011.05.001

Melsheimer, C., & Spreen, G. (2019). *AMSR2 ASI sea ice concentration data, Arctic, version 5.4 (NetCDF) (July 2012–December 2019)* [Dat Set]. PANGAEA. https://doi.org/10.1594/PANGAEA.898399

Morison, J. H., Long, C. E., & Levine, M. D. (1985). Internal wave dissipation under sea ice. *Journal of Geophysical Research*, *90*(C6), 11959. https://doi.org/10.1029/jc090ic06p11959

Perovich, D., Meier, W., Tschudi, M., Hendricks, S., Petty, A. A., Divine, D., et al. (2020). *Sea ice*. https://doi.org/10.25923/n170-9h57

Pinkel, R. (2005). Near-inertial wave propagation in the western Arctic. *Journal of Physical Oceanography*, *35*(5), 645–665. https://doi.org/10.1175/JPO2715.1

Polyakov, I. V., Rippeth, T. P., Fer, I., Baumann, T. M., Carmack, E. C., Ivanov, V. V., et al. (2020). Intensification of near-surface currents and shear in the Eastern Arctic Ocean. *Geophysical Research Letters*, *47*(16), 1–9. https://doi.org/10.1029/2020GL089469

Polzin, K., Kunze, E., Hummon, J., & Firing, E. (2002). The finescale response of lowered ADCP velocity profiles. *Journal of Atmospheric and Oceanic Technology*, *19*(2), 205–224. https://doi.org/10.1175/1520-0426(2002)019<0205:TFROLA>2.0.CO;2

Polzin, K. L., Naveira Garabato, A. C., Huussen, T. N., Sloyan, B. M., & Waterman, S. (2014). Finescale parameterizations of turbulent dissipation. *Journal of Geophysical Research: Oceans*, *119*(2), 1383–1419. https://doi.org/10.1002/2013JC008979

Polzin, K. L., Toole, J. M., & Schmit, R. W. (1995). Finescale parameterizations of turbulent dissipation. *Journal of Physical Oceanography*, *25*(3), 306–328. https://doi.org/10.1175/1520-0485(1995)025<0306:fpotd>2.0.co;2

Proshutinsky, A., Krishfield, R., Toole, J. M., Timmermans, M. L., Williams, W., Zimmermann, S., et al. (2019). Analysis of the Beaufort Gyre freshwater content in 2003–2018. *Journal of Geophysical Research: Oceans*, *124*(12), 9658–9689. https://doi.org/10.1029/2019JC015281

Rainville, L., Lee, C. M., & Woodgate, R. A. (2011). Impact of wind-driven mixing in the Arctic Ocean. *Oceanography*, *24*(3), 136–145. https://doi.org/10.5670/oceanog.2011.65

Rainville, L., & Woodgate, R. A. (2009). Observations of internal wave generation in the seasonally ice-free Arctic. *Geophysical Research Letters*, *36*(23), 1–5. https://doi.org/10.1029/2009GL041291

Rippeth, T. P., Lincoln, B. J., Lenn, Y. D., Green, J. A., Sundfjord, A., & Bacon, S. (2015). Tide-mediated warming of Arctic halocline by Atlantic heat fluxes over rough topography. *Nature Geoscience*, *8*(3), 191–194. https://doi.org/10.1038/ngeo2350

Rippeth, T. P., Vlasenko, V., Stashchuk, N., Scannell, B. D., Green, J. A., Lincoln, B. J., & Bacon, S. (2017). Tidal conversion and mixing Poleward of the critical latitude (an Arctic case study). *Geophysical Research Letters*, *44*(24), 12349–12357. https://doi.org/10.1002/2017GL075310

Shaw, W. J., Stanton, T. P., McPhee, M. G., Morison, J. H., & Martinson, D. G. (2009). Role of the upper ocean in the energy budget of Arctic sea ice during SHEBA. *Journal of Geophysical Research*, *114*(6), 1–21. https://doi.org/10.1029/2008JC004991

Shibley, N. C., Timmermans, M.-L., Carpenter, J. R., & Toole, J. M. (2017). Spatial variability of the Arctic Ocean's double-diffusive staircase. *Journal of Geophysical Research: Oceans*, *122*(2), 980–994. https://doi.org/10.1002/2016JC012419

Silverthorne, K. E., & Toole, J. M. (2009). Seasonal kinetic energy variability of near-inertial motions. *Journal of Physical Oceanography*, *39*(4), 1035–1049. https://doi.org/10.1175/2008JPO3920.1

Spreen, G., Kaleschke, L., & Heygster, G. (2008). Sea ice remote sensing using AMSR-E 89-GHz channels. *Journal of Geophysical Research*, *113*(2), 1–14. https://doi.org/10.1029/2005JC003384

Steele, M., Morison, J., Ermold, W., Rigor, I., Ortmeyer, M., & Shimada, K. (2004). Circulation of summer Pacific halocline water in the Arctic Ocean. *Journal of Geophysical Research*, *109*(2), 1–18. https://doi.org/10.1029/2003jc002009

Stroeve, J. C., Serreze, M. C., Holland, M. M., Kay, J. E., Malanik, J., & Barrett, A. P. (2012). The Arctic's rapidly shrinking sea ice cover: A research synthesis. *Climatic Change*, *110*(3–4), 1005–1027. https://doi.org/10.1007/s10584-011-0101-1

Sutherland, B. R. (2016). Internal wave transmission through a thermohaline staircase. *Physical Review Fluids*, *1*(1), 1–13. https://doi.org/10.1103/PhysRevFluids.1.013701

Timmermans, M., Proshutinsky, A., Golubeva, E., Jackson, J. M., Krishfield, R., McCall, M., et al. (2014). Mechanisms of Pacific summer water variability in the Arctic's central Canada Basin. *Journal of Geophysical Research: Oceans*, *119*(11), 7523–7548. https://doi.org/10.1002/2014JC010273

Timmermans, M., Toole, J., Krishfield, R., & Winsor, P. (2008). Ice-Tethered Profiler observations of the double-diffusive staircase in the Canada Basin thermocline. *Journal of Geophysical Research*, *113*, 1–10. https://doi.org/10.1029/2008jc004829

Timmermans, M. L., Marshall, J., Proshutinsky, A., & Scott, J. (2017). Seasonally derived components of the Canada Basin halocline. *Geophysical Research Letters*, *44*(10), 5008–5015. https://doi.org/10.1002/2017GL073042

Timmermans, M. L., Toole, J., & Krishfield, R. (2018). Warming of the interior Arctic Ocean linked to sea ice losses at the basin margins. *Science Advances*, *4*(8), 1–7. https://doi.org/10.1126/sciadv.aat6773

Toole, J. M., Timmermans, M. L., Perovich, D. K., Krishfield, R. A., Proshutinsky, A., & Richter-Menge, J. A. (2010). Influences of the ocean surface mixed layer and thermohaline stratification on Arctic Sea ice in the central Canada Basin. *Journal of Geophysical Research*, *115*(10), 1–14. https://doi.org/10.1029/2009JC005660

Waterhouse, A. F., Mackinnon, J. A., Nash, J. D., Alford, M. H., Kunze, E., Simmons, H. L., et al. (2014). Global patterns of diapycnal mixing from measurements of the turbulent dissipation rate. *Journal of Physical Oceanography*, *44*(7), 1854–1872. https://doi.org/10.1175/JPO-D-13-0104.1

Whalen, C. B., MacKinnon, J. A., Talley, L. D., & Waterhouse, A. F. (2015). Estimating the mean diapycnal mixing using a finescale strain parameterization. *Journal of Physical Oceanography*, *45*(4), 1174–1188. https://doi.org/10.1175/JPO-D-14-0167.1

WMO. (1970). *WMO sea ice nomenclature* (Tech. Rep., Vol. 259).